

Resonant self-force effects in extreme-mass-ratio binaries: A scalar modelZachary Nasipak^{1,2,3*} and Charles R. Evans³¹*NASA Goddard Space Flight Center, 8800 Greenbelt Road, Greenbelt, Maryland 20771, USA*²*Institute for Computational and Experimental Research in Mathematics, Brown University, Providence, Rhode Island 02903, USA*³*Department of Physics and Astronomy, University of North Carolina, Chapel Hill, North Carolina 27599, USA*

(Received 4 June 2021; accepted 27 July 2021; published 1 October 2021)

Extreme-mass-ratio inspirals (EMRIs), compact binaries with small mass-ratios $\epsilon \ll 1$, will be important sources for low-frequency gravitational wave detectors. Almost all EMRIs will evolve through important transient orbital $r\theta$ resonances, which will enhance or diminish their gravitational wave flux, thereby affecting the phase evolution of the waveforms at $O(\epsilon^{1/2})$ relative to leading order. While modeling the local gravitational self-force (GSF) during resonances is essential for generating accurate EMRI waveforms, so far the full GSF has not been calculated for an $r\theta$ -resonant orbit owing to computational demands of the problem. As a first step we employ a simpler model, calculating the scalar self-force (SSF) along $r\theta$ -resonant geodesics in Kerr spacetime. We demonstrate two ways of calculating the $r\theta$ -resonant SSF (and likely GSF), with one method leaving the radial and polar motions initially independent as if the geodesic is nonresonant. We illustrate results by calculating the SSF along geodesics defined by three $r\theta$ -resonant ratios (1:3, 1:2, 2:3). We show how the SSF and averaged evolution of the orbital constants vary with the initial phase at which an EMRI enters resonance. We then use our SSF data to test a previously proposed integrability conjecture, which argues that conservative effects vanish at adiabatic order during resonances. We find prominent contributions from the conservative SSF to the secular evolution of the Carter constant $\langle \dot{Q} \rangle$, but these nonvanishing contributions are on the order of, or less than, the estimated uncertainties of our self-force results. The uncertainties come from residual incomplete removal of the singular field in the regularization process. Higher order regularization parameters, once available, will allow definitive tests of the integrability conjecture.

DOI: [10.1103/PhysRevD.104.084011](https://doi.org/10.1103/PhysRevD.104.084011)**I. INTRODUCTION**

The future LISA space mission [1,2] will build upon the success of current ground-based detectors by observing new gravitational wave sources in the milli-Hertz band [3–5]. Among these new sources are extreme-mass-ratio inspirals (EMRIs): binaries composed of a stellar-mass compact object ($\mu \sim 10 M_\odot$) in bound orbit about a massive black hole ($M \sim 10^6 M_\odot$). With their small mass ratios ($\epsilon \equiv \mu/M \ll 1$), EMRIs evolve adiabatically due to orbit-averaged gravitational wave fluxes, with the smaller secondary body completing $\sim 10^5$ orbits around the more massive primary as the binary emits gravitational waves visible to low-frequency detectors. As a result of their long durations, EMRI signals are expected to have cumulative signal-to-noise ratios (SNRs) of several tens to several hundreds, allowing high-precision measurements that exceed the capabilities of current ground-based gravitational wave observatories [5,6]. Such high SNR measurements will still

require accurate waveform models to assist in detecting events and in measuring physical source parameters [7].

EMRIs are naturally modeled within the framework of black hole perturbation theory (BHPT), in which the small compact object is treated as a perturbing body in the stationary background spacetime associated with the primary black hole [8,9]. On the orbital timescale $T_{\text{orb}} \sim M$, the dynamics of the small body closely approximates a geodesic with a trio of fundamental frequencies (the radial frequency Ω_r , polar frequency Ω_θ , and azimuthal frequency Ω_ϕ) [10–12]. However, as the system evolves the small body is gradually pushed away from this geodesic as it interacts with its own gravitational perturbation. This behavior is typically described in terms of a local gravitational self-force (GSF) [13,14] that acts on the secondary and, at leading perturbative-order, makes an $O(\epsilon)$ correction to its motion. The dissipative piece of the GSF drives the adiabatic inspiral of the secondary, while the conservative piece provides nonsecular perturbations to the motion. The secular effect of the averaged dissipative GSF dominates the phase evolution of the orbit, which accumulates like $\sim \epsilon^{-1}$ at leading

*zachary.nasipak@nasa.gov

adiabatic order. This defines the inspiral or radiation timescale $T_{\text{tr}} \sim M\epsilon^{-1}$, over which the orbital frequencies undergo order-unity fractional changes. Furthermore, at a more subtle level, perturbations due to the oscillatory part of the dissipative and conservative GSF produce small shifts in the orbital frequencies that affect the orbit and cumulative phase at a level $O(\epsilon)$ relative to the leading-order adiabatic inspiral [15]. This correction is the post-1 adiabatic order effect.

In almost all astrophysically-relevant EMRIs, the evolution of the orbital frequencies due to the GSF will cause these systems to pass through one or more consequential orbital resonances at some point in their observed inspirals [16,17]. An orbital resonance occurs when at least two frequencies of orbital motion, Ω_1 and Ω_2 , form a rational ratio, i.e., $\Omega_2/\Omega_1 = \beta_2/\beta_1$ with coprime $\beta_1, \beta_2 \in \mathbb{Z}$. The smaller that the integers β_1 and β_2 are, the stronger the resonance. In the solar system, orbital resonances commonly occur among satellites sharing the same primary, such as the 2:3 resonance of Neptune and Pluto and the 1:2 resonance of the Galilean satellites Io and Europa.

For EMRIs, resonances can form between any two of the three frequencies of the smaller body's orbital motion, with different resonant combinations leading to different physical effects.¹ For instance, $r\varphi$ [22] and $\theta\varphi$ resonances [23] can lead to anisotropic radiation of gravitational waves, resulting in resonant “kicks” to the velocity of an EMRI's center-of-mass. Such effects are expected to contribute to an EMRI's phase evolution and waveform at $O(\epsilon^{3/2})$ relative to adiabatic order (i.e., post- $\frac{3}{2}$ adiabatic order) [22]. Because LISA waveforms require a phase accuracy of ~ 0.1 radians, $r\varphi$ and $\theta\varphi$ resonances are presumably safe to neglect at present in EMRI models. On the other hand, $r\theta$ resonances, which only arise in EMRIs with Kerr primaries, will enhance or diminish the time-averaged gravitational wave flux, thereby influencing the evolution of the frequencies Ω_r , Ω_θ , and Ω_φ (and similarly the orbital energy, angular momentum, and Carter constant) [17,24,25]. The strongest resonances will have frequency ratios such as 1:3, 1:2, or 2:3 [16,26] and will ordinarily persist for a resonant period $T_{\text{res}} \sim M\epsilon^{-1/2}$ [24]. Because these orbital resonances are expected to be transient,² their effect is at post- $\frac{1}{2}$ adiabatic order [24].³

Incorporating this new resonant timescale into evolutionary models poses difficulties with, for example, near-identity transformations [30] and multiscale expansions

¹See Refs. [18–20] for comprehensive lists of research focused on orbital resonances in Kerr spacetime and [18,21] for more general discussions of EMRI resonances.

²It may be possible for certain EMRIs to be caught in a sustained $r\theta$ resonance, but a system must meet stringent (if even possible) conditions for this to occur [19].

³While not the focus of this work, tidal resonances, which may occur for EMRIs that are perturbed by one or more external bodies, can experience similar post- $\frac{1}{2}$ adiabatic corrections to the phase evolution [27–29].

[20,21]. In effect, on a timescale just larger than T_{res} , an EMRI's orbital parameters appear to experience $O(\epsilon^{1/2})$ shifts or jumps in their values, as shown in [17,24]. These jumps, which are sensitive to the orbital phase of the EMRI as it enters resonance [25], lead to an overall $O(\epsilon^{-1/2})$ shift in the cumulative phase of the system. Failing to account for these resonant phase shifts may only slightly degrade EMRI detection rates [17], but it will introduce significant systematic biases to EMRI parameter estimation that will dominate over standard statistical errors [31]. Because nearly all EMRIs will encounter either a 1:3, 1:2, or 2:3 $r\theta$ resonance as they emit gravitational wave signals in the LISA passband [16], properly modeling transient $r\theta$ resonances is essential to producing subradian phase-accurate waveforms for the detection and characterization of EMRIs by LISA.

To date, numerical investigations of transient $r\theta$ resonances have not incorporated local strong-field conservative perturbations [17,24,25,31]. While conservative perturbations vanish at adiabatic order for nonresonant motion, it is not yet known if they may contribute to the adiabatic evolution of EMRIs during $r\theta$ resonances. Flanagan and Hinderer [24] argue that conservative effects will not contribute at leading order during resonances based on their *integrability conjecture*.⁴ The validity of this conjecture remains unclear. Isoyama *et al.* [32,33] have found the presence of potential conservative contributions to the evolution of the orbit-averaged Carter constant through their Hamiltonian formulation of EMRI dynamics. For the integrability conjecture to hold, these terms would have to vanish when integrated over an entire orbit, which has not been demonstrated analytically.

The integrability conjecture can potentially be tested through numerical calculations of conservative quantities, such as a computation of the local GSF in Kerr spacetime during an $r\theta$ resonance. First-order GSF calculations for generic bound orbits about a Schwarzschild black hole are well advanced, to the point of allowing long-term evolutionary computations [30,34–36]. Indeed, even second-order GSF calculations for restricted orbits in Schwarzschild are now emerging [37]. Recent work by van de Meent provided the first GSF results for generic orbits in a Kerr EMRI [38]. However, these calculations are much more computationally demanding than their Schwarzschild counterparts, and long-term self-forced evolutions of Kerr EMRIs have not yet been produced. Not even snapshots of the GSF in Kerr EMRIs during $r\theta$ resonances have been attempted.

Thus, as a first step in exploring local radiation-reaction effects driven by resonances, we consider a scalar field analogue and calculate the scalar self-force (SSF) that arises due to a bound particle with scalar charge q in an $r\theta$ resonance about a Kerr black hole. This work builds off of a

⁴We follow [25] in referring to Flanagan and Hinderer's argument as the integrability conjecture.

previous paper [39], in which we presented the first calculation of the SSF for nonresonant inclined eccentric orbits in Kerr spacetime. By treating $q^2/(\mu M)$ as a small parameter, this SSF model mimics the GSF problem. As is common for adiabatic and osculating geodesic evolutions, we assume the motion of the particle to be exactly geodesic and calculate the resulting *geodesic scalar self-force*. This assumption produces an error that is on the order of the time-averaged dissipative part of the second-order self-force. In this work we are not yet concerned with applying the self-force and calculating a portion of the evolution based on the backreaction.

To set notation, in Sec. II we review nonresonant and resonant geodesics in Kerr spacetime, along with various parametrizations of geodesic functions. In Sec. III we review the scalar self-force model presented in [39]. In Sec. IV, we extend our previous methods for calculating the SSF along nonresonant orbits to the case of $r\theta$ resonances by making use of a simple shifting relation based on symmetries (Killing vectors) of the Kerr spacetime. In Sec. V, we numerically calculate the SSF experienced by a scalar-charged particle for six different $r\theta$ -resonant geodesics. We use these results in Sec. VI to compute the secular evolution (orbit-averaged time rate-of-change) of the orbital constants (e.g., $\langle \dot{\mathcal{E}} \rangle$, $\langle \dot{\mathcal{L}}_z \rangle$, $\langle \dot{\mathcal{Q}} \rangle$). We demonstrate that the conservative components of the SSF do not contribute to the evolution of the orbital energy and angular momentum $\langle \dot{\mathcal{E}} \rangle$ and $\langle \dot{\mathcal{L}}_z \rangle$, respectively, as expected from flux-balance arguments. We do find nonzero contributions from the conservative SSF to the secular evolution of the Carter constant $\langle \dot{\mathcal{Q}} \rangle$, though these contributions are consistent with the level of systematic numerical errors produced by our regularization scheme. We conclude with

a discussion of these results in Sec. VII. Because we only focus on $r\theta$ resonances in this work, henceforth we will occasionally refer to these as simply resonances. For this paper we use units such that $c = G = 1$, use metric signature $(-+++)$, and sign conventions, where applicable, of Misner, Thorne, and Wheeler [40].

II. GEODESICS AND RESONANT MOTION IN KERR SPACETIME

The instantaneous motion of a small mass orbiting a much more massive rotating black hole is approximated by that of a bound timelike geodesic in Kerr spacetime. This is the zeroth-order motion in BHPT. Bound Kerr geodesics librate at different frequencies in the radial and polar directions, as shown in the left panel of Fig. 1. Generally, the instantaneous periods of a Kerr EMRI's radial and polar motions are incommensurate. In these circumstances, the geodesic is ergodic: given an infinite time, the motion passes through every point in a finite bounded region in r and θ . For certain orbital parameters, however, these radial and polar periods will be in a rational-number ratio, giving rise to a resonance. In these cases the motion is not ergodic. Instead, it loops back on itself, and it does not fill the corresponding bounded region in r and θ [41] (see the right panel of Fig. 1).

To better understand these different behaviors, and to establish notation, we review the analytic framework for studying bound geodesics in the Kerr spacetime, primarily following the work of [10,11,25,40,42,43], though we have consolidated and adapted notation for consistency. We also discuss various prescriptions for parametrizing geodesics and how those parametrizations must be handled when describing resonances.

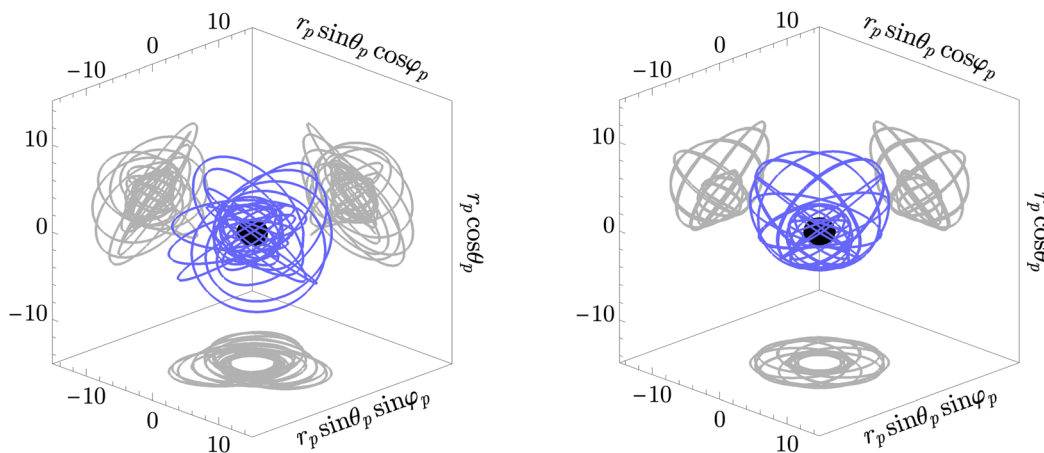


FIG. 1. Inclined eccentric geodesics around a Kerr black hole with spin $a/M = 0.9$ and mass $M = 1$. The plot on the left is a nonresonant geodesic with orbital parameters $(p, e, x) = (4.700, 0.5, \cos \pi/4)$. The plot on the right, in contrast, is a 1:2 $r\theta$ -resonant geodesic with orbital parameters $(p, e, x) \simeq (4.607, 0.5, \cos \pi/4)$. The semilatus rectum p is truncated at four significant digits and specifically chosen so that the particle undergoes one radial libration for every two polar librations. The solid (blue) curves trace out the three-dimensional motion of the two geodesics in Boyer-Lindquist coordinates (r, θ, φ) . The solid (grey) curves show various two-dimensional projections of the three-dimensional orbit.

A. Separation of the geodesic equations

Consider a point particle with mass μ on a bound geodesic $x_p^\mu(\tau)$ with four-velocity $u^\alpha \equiv dx_p^\alpha/d\tau$, where τ is the particle's proper time. The background spacetime, described by the metric $g_{\alpha\beta}$, is parametrized by the black hole spin a and mass M . Adopting Boyer-Lindquist coordinates (t, r, θ, φ) , the Kerr line element reads

$$ds^2 = -\left(1 - \frac{2Mr}{\Sigma}\right)dt^2 + \frac{\Sigma}{\Delta}dr^2 - \frac{4Mar\sin^2\theta}{\Sigma}dt d\varphi + \Sigma d\theta^2 + \frac{\sin^2\theta}{\Sigma}(\varpi^4 - a^2\Delta\sin^2\theta)d\varphi^2, \quad (2.1)$$

where $\Sigma \equiv r^2 + a^2 \cos^2\theta$, $\Delta \equiv r^2 - 2Mr + a^2$, and $\varpi^2 \equiv r^2 + a^2$.

Geodesic motion in Kerr spacetime is completely integrable, leading to three constants of motion—the specific energy \mathcal{E} , the z component of the specific angular momentum \mathcal{L}_z , and the (scaled) Carter constant \mathcal{Q} [42]—all of which can be related to the Killing symmetries of Kerr. The specific energy and angular momentum correspond to the Killing vectors $\xi_{(t)}^\mu$ and $\xi_{(\varphi)}^\mu$,

$$\mathcal{E} \equiv -\xi_{(t)}^\mu u_\mu = -u_t, \quad (2.2)$$

$$\mathcal{L}_z \equiv +\xi_{(\varphi)}^\mu u_\mu = +u_\varphi, \quad (2.3)$$

while the Carter constant is associated with the Killing tensor $K^{\mu\nu}$ [44],

$$\mathcal{Q} \equiv K^{\mu\nu} u_\mu u_\nu - (\mathcal{L}_z - a\mathcal{E})^2, \quad (2.4)$$

which is discussed further in Appendix C 3.

Introducing the (Carter-)Mino time parameter λ [8,11,40,42], defined by $d\lambda \equiv \Sigma_p^{-1} d\tau$, the geodesic equations separate

$$\frac{dt_p}{d\lambda} = V_{tr}(r_p) + V_{t\theta}(\theta_p), \quad (2.5)$$

$$\frac{dr_p}{d\lambda} = \pm \sqrt{V_r(r_p)}, \quad (2.6)$$

$$\frac{d\theta_p}{d\lambda} = \pm \sqrt{V_\theta(\theta_p)}, \quad (2.7)$$

$$\frac{d\varphi_p}{d\lambda} = V_{\varphi r}(r_p) + V_{\varphi\theta}(\theta_p), \quad (2.8)$$

where the various V functions are defined in [11,39], and the subscript p denotes that a function is evaluated on the particle's worldline x_p^μ .

Rather than specifying a geodesic by directly choosing values for \mathcal{E} , \mathcal{L}_z , and \mathcal{Q} , we use relativistic definitions of

semilatus rectum p and orbital eccentricity e that are analogous to those of Keplerian orbits,

$$p \equiv \frac{2r_{\min}r_{\max}}{M(r_{\max} + r_{\min})}, \quad e \equiv \frac{r_{\max} - r_{\min}}{r_{\max} + r_{\min}}. \quad (2.9)$$

We add to that the projection of the orbital inclination

$$x \equiv \cos\left(\frac{\pi}{2} - \theta_{\min}\right), \quad (2.10)$$

to round out the parametrization of the orbits. Here, r_{\min} and r_{\max} are the minimum and maximum radii reached by the point mass, and $\theta_{\min} = \pi - \theta_{\max}$ is its minimum polar angle. These are the turning points of the geodesic, where $V_r(r_{\min}) = V_r(r_{\max}) = V_\theta(\theta_{\min}) = V_\theta(\pi - \theta_{\min}) = 0$. Once p , e , and x are specified for an orbit, it is straightforward to determine the corresponding \mathcal{E} , \mathcal{L}_z , and \mathcal{Q} [10,45]. One can then solve (2.5)–(2.8) using spectral integration methods [39,46] or analytic special functions [12,45]. In this work we use a hybrid scheme: we sample the analytic geodesics solutions presented in [12], then construct their discrete Fourier representations, which provide an exponentially-convergent numerical approximation of the geodesics.

B. Frequencies of generic bound motion

For inclined eccentric (bound) geodesics the point mass librates in r and θ with radial and polar Mino time periods

$$\Lambda_r \equiv 2 \int_{r_{\min}}^{r_{\max}} \frac{dr}{\sqrt{V_r(r)}}, \quad (2.11)$$

$$\Lambda_\theta \equiv 2 \int_{\theta_{\min}}^{\pi - \theta_{\min}} \frac{d\theta}{\sqrt{V_\theta(\theta)}}, \quad (2.12)$$

and corresponding Mino time frequencies

$$\Upsilon_r \equiv \frac{2\pi}{\Lambda_r}, \quad \Upsilon_\theta \equiv \frac{2\pi}{\Lambda_\theta}. \quad (2.13)$$

In Kerr spacetime, Υ_θ is always greater than Υ_r for bound motion. The time and azimuthal locations, which depend on the radial and polar motions [see (2.5) and (2.8)], accumulate at average rates in λ denoted by Γ and Υ_φ and are given by

$$\Gamma = \frac{1}{\Lambda_r} \int_0^{\Lambda_r} V_{tr}(r_p) d\lambda + \frac{1}{\Lambda_\theta} \int_0^{\Lambda_\theta} V_{t\theta}(\theta_p) d\lambda, \quad (2.14)$$

$$\Upsilon_\varphi = \frac{1}{\Lambda_r} \int_0^{\Lambda_r} V_{\varphi r}(r_p) d\lambda + \frac{1}{\Lambda_\theta} \int_0^{\Lambda_\theta} V_{\varphi\theta}(\theta_p) d\lambda, \quad (2.15)$$

where r_p and θ_p are understood to be functions of λ . Together, these form the complete set of Mino time

frequencies $\Upsilon_\alpha = (\Gamma, \Upsilon_r, \Upsilon_\theta, \Upsilon_\varphi)$. They are related to the fundamental coordinate-time frequencies by

$$\Omega_r = \frac{\Upsilon_r}{\Gamma}, \quad \Omega_\theta = \frac{\Upsilon_\theta}{\Gamma}, \quad \Omega_\varphi = \frac{\Upsilon_\varphi}{\Gamma}, \quad (2.16)$$

which then define the discrete frequencies

$$\omega_{mkn} \equiv m\Omega_\varphi + k\Omega_\theta + n\Omega_r, \quad (2.17)$$

in the multiperiodic Fourier spectrum of any variable made time dependent by the geodesic motion. Note that these coordinate-time frequencies Ω_α do not uniquely define a geodesic due to the existence of isofrequency pairings [47], though it is well argued that (up to initial conditions) geodesics are uniquely defined by their Mino time frequencies Υ_α [19].

C. Analytic structure of geodesic solutions and their dependence on initial conditions

We consider next families of geodesics and their dependence on initial conditions. Let an inclined eccentric geodesic be parametrized by λ , $\hat{x}^\mu = \hat{x}_p^\mu(\lambda)$, and have the following initial conditions:

$$\hat{x}_p^\mu(0) = (0, r_{\min}, \theta_{\min}, 0), \quad (2.18)$$

$$\hat{u}^r(0) = \hat{u}^\theta(0) = 0. \quad (2.19)$$

Following the nomenclature of [11], we refer to a trajectory with these initial conditions as a fiducial geodesic and distinguish it with a hat. Integrating (2.5)–(2.8) and enforcing these fiducial initial conditions, the periodicity in the motion gives rise to solutions that have the form

$$\hat{t}_p(\lambda) = \Gamma\lambda + \Delta\hat{t}^{(r)}(\Upsilon_r\lambda) + \Delta\hat{t}^{(\theta)}(\Upsilon_\theta\lambda), \quad (2.20)$$

$$\hat{r}_p(\lambda) = r_{\min} + \Delta\hat{r}^{(r)}(\Upsilon_r\lambda), \quad (2.21)$$

$$\hat{\theta}_p(\lambda) = \theta_{\min} + \Delta\hat{\theta}^{(\theta)}(\Upsilon_\theta\lambda), \quad (2.22)$$

$$\hat{\varphi}_p(\lambda) = \Upsilon_\varphi\lambda + \Delta\hat{\varphi}^{(r)}(\Upsilon_r\lambda) + \Delta\hat{\varphi}^{(\theta)}(\Upsilon_\theta\lambda), \quad (2.23)$$

where the various $\Delta\hat{x}$ terms are oscillatory periodic functions. Here we use $\Delta\hat{x}$ to represent $\Delta\hat{t}$, $\Delta\hat{r}$, $\Delta\hat{\theta}$, and $\Delta\hat{\varphi}$, which have the following properties:

$$\Delta\hat{x}^{(r)}(2\pi + \Upsilon_r\lambda) = \Delta\hat{x}^{(r)}(\Upsilon_r\lambda), \quad \Delta\hat{x}^{(r)}(0) = 0, \quad (2.24)$$

$$\Delta\hat{x}^{(\theta)}(2\pi + \Upsilon_\theta\lambda) = \Delta\hat{x}^{(\theta)}(\Upsilon_\theta\lambda), \quad \Delta\hat{x}^{(\theta)}(0) = 0. \quad (2.25)$$

Furthermore, from the way a fiducial geodesic is defined, all of these periodic functions are either even or odd with respect to $\lambda = 0$, with $\Delta\hat{t}$ and $\Delta\hat{\varphi}$ being odd

(antisymmetric) and $\Delta\hat{r}^{(r)}$ and $\Delta\hat{\theta}^{(\theta)}$ being even (symmetric). Exact definitions of these geodesic functions are provided in [11,12,39].

Next, we consider an inclined eccentric geodesic $x_p^\mu(\lambda)$ with arbitrary initial conditions

$$x_p^\mu(0) = (t_0, r_0, \theta_0, \varphi_0), \quad (2.26)$$

$$u^r(0) = u_0^r, \quad u^\theta(0) = u_0^\theta. \quad (2.27)$$

An arbitrary geodesic can be expressed in terms of the fiducial solutions by shifting the arguments of the periodic functions,

$$\begin{aligned} t_p(\lambda; t_0, \lambda_0^{(r)}, \lambda_0^{(\theta)}) &= t_0 - \Delta\hat{t}(\Upsilon_r\lambda_0^{(r)}, \Upsilon_\theta\lambda_0^{(\theta)}) + \Gamma\lambda \\ &\quad + \Delta\hat{t}(\Upsilon_r(\lambda + \lambda_0^{(r)}), \Upsilon_\theta(\lambda + \lambda_0^{(\theta)})), \end{aligned} \quad (2.28)$$

$$r_p(\lambda; \lambda_0^{(r)}) = r_{\min} + \Delta\hat{r}^{(r)}(\Upsilon_r\lambda + \Upsilon_r\lambda_0^{(r)}), \quad (2.29)$$

$$\theta_p(\lambda; \lambda_0^{(\theta)}) = \theta_{\min} + \Delta\hat{\theta}^{(\theta)}(\Upsilon_\theta\lambda + \Upsilon_\theta\lambda_0^{(\theta)}), \quad (2.30)$$

$$\begin{aligned} \varphi_p(\lambda; \varphi_0, \lambda_0^{(r)}, \lambda_0^{(\theta)}) &= \varphi_0 - \Delta\hat{\varphi}(\Upsilon_r\lambda_0^{(r)}, \Upsilon_\theta\lambda_0^{(\theta)}) + \Upsilon_\varphi\lambda \\ &\quad + \Delta\hat{\varphi}(\Upsilon_r(\lambda + \lambda_0^{(r)}), \Upsilon_\theta(\lambda + \lambda_0^{(\theta)})). \end{aligned} \quad (2.31)$$

In the above expressions, we introduced the compact notation,

$$\Delta\hat{t}(\Upsilon_r\lambda, \Upsilon_\theta\tilde{\lambda}) \equiv \Delta\hat{t}^{(r)}(\Upsilon_r\lambda) + \Delta\hat{t}^{(\theta)}(\Upsilon_\theta\tilde{\lambda}), \quad (2.32)$$

$$\Delta\hat{\varphi}(\Upsilon_r\lambda, \Upsilon_\theta\tilde{\lambda}) \equiv \Delta\hat{\varphi}^{(r)}(\Upsilon_r\lambda) + \Delta\hat{\varphi}^{(\theta)}(\Upsilon_\theta\tilde{\lambda}), \quad (2.33)$$

for the sums of the radial and polar dependencies of the time and azimuthal components. The initial orbital offsets, $\lambda_0^{(r)}$ and $\lambda_0^{(\theta)}$, are defined in terms of the initial radial and polar positions and velocities by

$$\begin{aligned} \Delta\hat{r}^{(r)}(\Upsilon_r\lambda_0^{(r)}) &= r_0 - r_{\min}, & \text{sgn}(\sin \Upsilon_r\lambda_0^{(r)}) &= \text{sgn}u_0^r, \\ \Delta\hat{\theta}^{(\theta)}(\Upsilon_\theta\lambda_0^{(\theta)}) &= \theta_0 - \theta_{\min}, & \text{sgn}(\sin \Upsilon_\theta\lambda_0^{(\theta)}) &= \text{sgn}u_0^\theta. \end{aligned}$$

Here, sgn represents the sign function. The fiducial case is recovered by setting $t_0 = \varphi_0 = \lambda_0^{(r)} = \lambda_0^{(\theta)} = 0$.

All bound geodesics can be described by (2.28)–(2.31), though any geodesic that passes through a simultaneous minimum in the radial and polar motion (i.e., $r_p = r_{\min}$ and $\theta_p = \theta_{\min}$) can be mapped to a fiducial geodesic via trivial offsets in t_0 and φ_0 . As long as there exist integers k' and n' such that

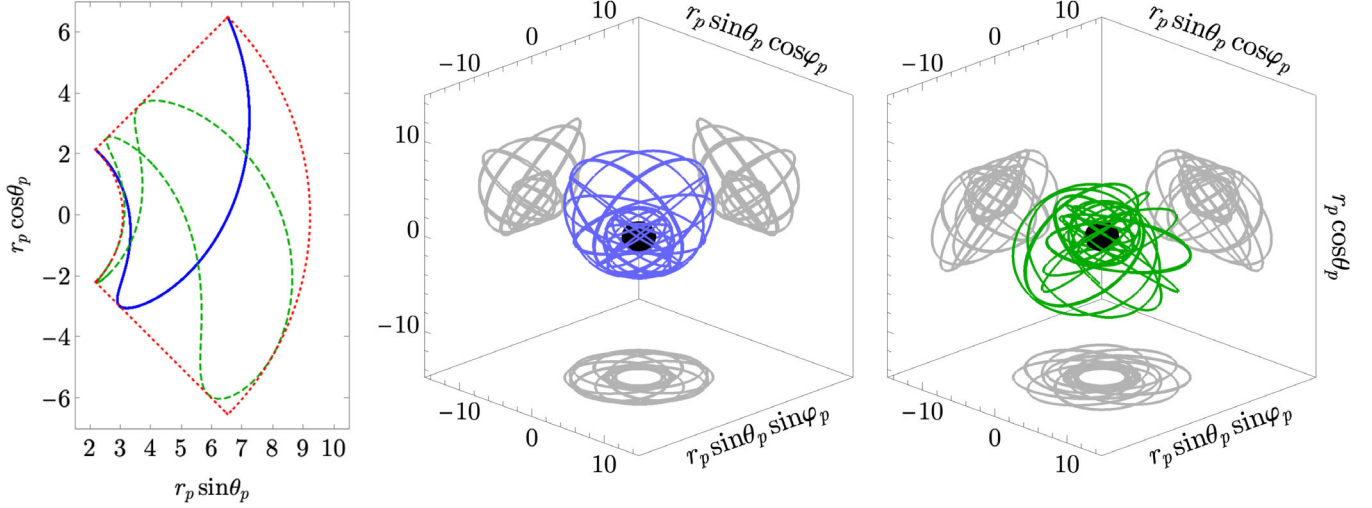


FIG. 2. Projected motion for two 1:2 $r\theta$ -resonant geodesics around a Kerr black hole with spin $a/M = 0.9$ and mass $M = 1$. The left plot suppresses the azimuthal motion and depicts the radial and polar motion of both geodesics in the poloidal plane. Three-dimensional projections of these two geodesics are mapped separately in the center and right plots. Both geodesics share the orbital parameters $(p, e, x) \approx (4.607, 0.5, \cos \pi/4)$ and the same $r\theta$ -resonant frequencies. While they both start at $r_p(0) = r_{\min}$, they differ in their initial polar positions and polar velocities. The solid (blue) line in the left plot and the center plot trace out a geodesic with the initial offset $\lambda_0^{(\theta)} = 0$ ($q_{\theta 0} = \bar{q}_0 = 0$), while the dashed (green) line in the left plot and the far right plot represent a geodesic with the initial offset $\lambda_0^{(\theta)} = -3\Lambda_\theta/8$ ($q_{\theta 0} = \beta_\theta \bar{q}_0 = -3\pi/4$). The motion for each plot is shown from $\lambda = 0$ to $\lambda = 47$.

$$\lambda_0^{(\theta)} - \lambda_0^{(r)} = n'\Lambda_r - k'\Lambda_\theta, \quad (2.34)$$

$$\omega_{mN} \equiv m\Omega_\varphi + N\Omega, \quad (2.36)$$

is satisfied, then a simultaneous turning point at these minimum positions will occur.⁵ Because nonresonant eccentric inclined geodesics are ergodic, this simultaneous turning point always exists (i.e., on a long enough timescale) and, therefore, nonresonant geodesics can be described by the fiducial expressions in (2.20)–(2.23), without loss of generality up to a trivial shifting of Mino time λ .

D. Special case of $r\theta$ -resonant geodesics

We classify $r\theta$ resonances in terms of the (relatively prime) integers β_r and β_θ that define the ratio between the radial and polar frequencies, i.e.,

$$\frac{\Omega_r}{\Omega_\theta} = \frac{\beta_r}{\beta_\theta}. \quad (2.35)$$

Low-integer ratios (i.e., ones with small integers like $\beta_r:\beta_\theta = 1:2, 2:3$) are referred to as strong resonances, while high-integer ratios (e.g., 10:11, 1:20) are weak resonances. Because the radial and polar frequencies are commensurate during an $r\theta$ resonance, the discrete frequency spectrum of resonant geodesics reduces to

⁵A similar symmetry also exists for other simultaneous turning points [e.g., $(r_{\min}, \theta_{\max}), (r_{\max}, \theta_{\max})$], which leads to the alternate constraint of Eq. (4.9) in [11]. For simplicity we only focus on the case of a simultaneous minimum turning point $(r_{\min}, \theta_{\min})$, which is sufficient for our discussion.

where $\Omega \equiv \Omega_r/\beta_r = \Omega_\theta/\beta_\theta$ and $N \equiv k\beta_\theta + n\beta_r \in \mathbb{Z}$. In other words, for an $r\theta$ resonance the normally separate sets of harmonics of the radial and polar fundamental frequencies merge into one set of harmonics N , of a new lower net frequency Ω .

Resonant geodesics can also be described by (2.28)–(2.31). However, unlike nonresonant geodesics which are ergodic, $r\theta$ resonances follow restricted paths through the poloidal plane—as shown in Fig. 2—and these paths are sensitive to the initial conditions $\lambda_0^{(r)}$ and $\lambda_0^{(\theta)}$. For a resonance, the radial and polar motions oscillate with the shared (net) Mino time frequency and period

$$\Upsilon \equiv \frac{\Upsilon_r}{\beta_r} = \frac{\Upsilon_\theta}{\beta_\theta}, \quad \Lambda \equiv \beta_r\Lambda_r = \beta_\theta\Lambda_\theta. \quad (2.37)$$

For simultaneous minimum turning points to occur during a resonance, (2.34) reduces to the more stringent restriction that $\lambda_0^{(\theta)} - \lambda_0^{(r)} = N'\Lambda$, for some integer N' , which will not hold true for most choices of $\lambda_0^{(r)}$ and $\lambda_0^{(\theta)}$. Therefore, most resonant orbits cannot be mapped to the fiducial geodesic with the same frequencies.

Nevertheless, the symmetries of Kerr spacetime allow the same functions describing the fiducial orbit to be applied more broadly to the general resonant case. This process starts with defining the initial resonant offset $\lambda_0 \equiv \lambda_0^{(\theta)} - \lambda_0^{(r)}$. Any two $r\theta$ resonances that share the

same value of λ_0 (modulo Λ) can be mapped onto one another. Taking advantage of this mapping, one can simplify the description of geodesic orbits by setting $\lambda_0^{(r)}$ or $\lambda_0^{(\theta)}$ to 0. In this work, we choose $\lambda_0^{(r)} = 0$ so that $\lambda_0 = \lambda_0^{(\theta)}$, without loss of generality. The parametrization of the resonant motion in terms of the offset λ_0 is then

$$t_p(\lambda; \lambda_0) = \Gamma\lambda - \Delta\hat{t}(0, \beta_\theta \Upsilon\lambda_0) + \Delta\hat{t}(\beta_r \Upsilon\lambda, \beta_\theta \Upsilon(\lambda + \lambda_0)), \quad (2.38)$$

$$r_p(\lambda; \lambda_0) = r_{\min} + \Delta\hat{r}^{(r)}(\beta_r \Upsilon\lambda), \quad (2.39)$$

$$\theta_p(\lambda; \lambda_0) = \theta_{\min} + \Delta\hat{\theta}^{(\theta)}(\beta_\theta \Upsilon(\lambda + \lambda_0)), \quad (2.40)$$

$$\varphi_p(\lambda; \lambda_0) = \Upsilon_\varphi\lambda - \Delta\hat{\varphi}(0, \beta_\theta \Upsilon\lambda_0) + \Delta\hat{\varphi}(\beta_r \Upsilon\lambda, \beta_\theta \Upsilon(\lambda + \lambda_0)). \quad (2.41)$$

By varying the value of the offset in the range $0 \leq \lambda_0 < \Lambda$, we can generate all resonant paths through the poloidal plane that are characterized by the same orbital parameters and frequencies but have different initial positions (see Fig. 2).

E. Parametrizing geodesics with angle variables

The integrability of geodesic motion in Kerr spacetime also leads to a natural representation of the motion in terms of action-angle variables. This formalism forms the basis of

the two-timescale description of EMRI dynamics [15] and provides a characteristic parametrization for functions that depend on the librating radial and polar motions. The angle variable parametrization is also used for presenting gravitational self-force results [38], which we adopt in similar fashion.

The angle variables are related to λ by the Mino frequencies,

$$q_r = \Upsilon_r\lambda, \quad q_\theta = \Upsilon_\theta\lambda. \quad (2.42)$$

We similarly define the initial orbital phases

$$q_{(a)0} = \{q_{t0}, q_{r0}, q_{\theta0}, q_{\varphi0}\} = \{t_0, \Upsilon_r\lambda_0^{(r)}, \Upsilon_\theta\lambda_0^{(\theta)}, \varphi_0\}. \quad (2.43)$$

(Technically, for q_{t0} to represent a dimensionless phase it should be rescaled, i.e., Ωt_0 , but the distinction is unimportant for our present purposes.) Functions that are periodic with respect to the Mino time periods, Λ_r and Λ_θ , can then be parametrized in terms of the corresponding angle variables q_r and q_θ , e.g.,

$$\Delta\hat{r}^{(r)}(\Upsilon_r(\lambda + \lambda_0^{(r)})) \rightarrow \Delta\hat{r}^{(r)}(q_r + q_{r0}),$$

$$\Delta\hat{\theta}^{(\theta)}(\Upsilon_\theta(\lambda + \lambda_0^{(\theta)})) \rightarrow \Delta\hat{\theta}^{(\theta)}(q_\theta + q_{\theta0}).$$

Upon parametrizing functions in terms of the angle variables, it is straightforward to project function values

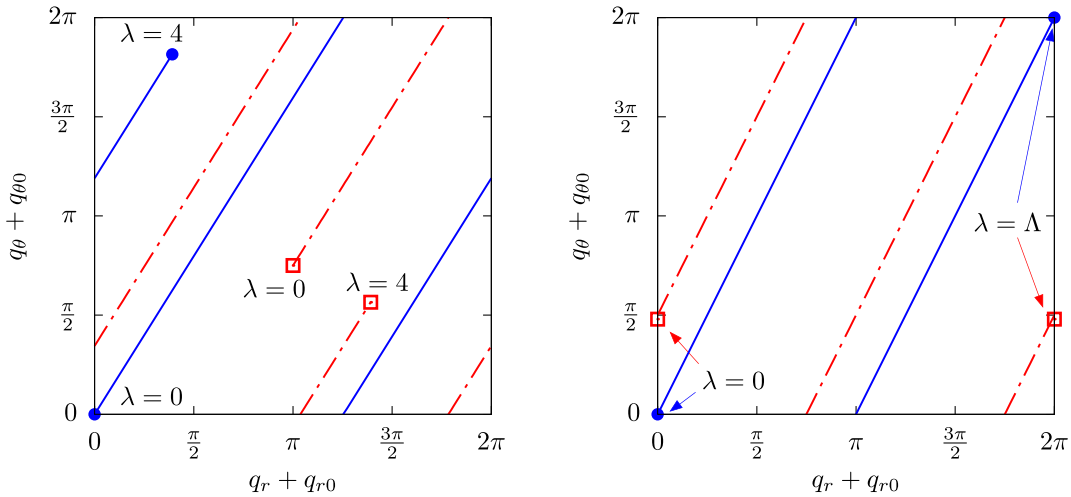


FIG. 3. Poloidal motion depicted on the torus for orbits with parameters $(a/M, p, e, x) = (0.9, 6, 0.5, \cos \pi/4)$ (left panel) and $(a/M, p, e, x) = (0.9, 4.607, 0.5, \cos \pi/4)$ (right panel). In the right plot parameters are chosen to generate a 1:2 $r:\theta$ resonance. The orbit in the left panel is nonresonant. There the solid (blue) line follows the path of a geodesic with fiducial initial conditions $q_{(a)0} = (t_0, q_{r0}, q_{\theta0}, \varphi_0) = (0, 0, 0, 0)$, while the dashed (red) line has initial conditions $q_{(a)0} = (0, 0, \pi/2, 0)$. (Both paths are plotted over the Mino time interval $\lambda \in [0, 4]$, with $M = 1$.) Given sufficient time, both paths will fill the entire torus and completely overlap. In the right panel the solid (blue) line follows the path of a geodesic with the initial resonant phase $\bar{q}_0 = 0$ on the Mino time interval $\lambda \in [0, \Lambda]$, where $\Lambda \simeq 4.494$ is the (net) resonant Mino time period. The dashed (red) line follows a geodesic with initial phase $\bar{q}_0 = \pi/2$ ($\theta_p(\lambda = 0) = \pi - \theta_{\min}$) on the same time interval. Unlike the nonresonant paths, the resonant geodesic flows in the right panel will never overlap with one another.

on the two-torus spanned by the two angle variables, such as the tori depicted in Fig. 3. Each (invariant) two-torus forms a section of configuration space for the radial and polar motion of the small body. The geodesic flow on the torus then describes the evolution of the motion through this configuration space, as discussed in [48]. For a nonresonant orbit, starting these paths at different points on the torus is equivalent to choosing different initial conditions. The effect of initial conditions on possible paths is shown in the top panel of Fig. 3. Given an infinite amount of Mino time, a system following a nonresonant geodesic will sample every point on the torus.

In the case of a resonance, the system executes a closed repeating motion through the domain, as seen in the bottom panel of Fig. 3. Choosing different initial positions on the torus can generate unique paths. The only way to sample all of the points on the torus is to consider an infinite number of resonant orbits that share the same frequencies Υ_α but different initial offsets λ_0 .

To distinguish resonant geodesics, we define a single angle variable \bar{q} for resonant motion and then a single angle parameter \bar{q}_0 for the initial resonant phase,⁶

$$\bar{q} \equiv \Upsilon\lambda = \frac{q_r}{\beta_r} = \frac{q_\theta}{\beta_\theta}, \quad \bar{q}_0 \equiv \Upsilon\lambda_0 = \frac{q_{\theta 0}}{\beta_\theta} - \frac{q_{r 0}}{\beta_r}. \quad (2.44)$$

In this mapping, \bar{q}_0 is a constant as the system evolves.

In terms of these resonant angles, we denote reparametrized functions with an overbar, such that

$$\Delta\bar{r}^{(r)}(\bar{q}) \equiv \Delta\hat{r}^{(r)}(\beta_r\bar{q}), \quad (2.45)$$

$$\Delta\bar{\theta}^{(\theta)}(\bar{q}; \bar{q}_0) \equiv \Delta\hat{\theta}^{(\theta)}(\beta_\theta\bar{q} + \beta_\theta\bar{q}_0), \quad (2.46)$$

$$\Delta\bar{t}(\bar{q}; \bar{q}_0) \equiv \Delta\hat{t}(\beta_r\bar{q}, \beta_\theta\bar{q} + \beta_\theta\bar{q}_0), \quad (2.47)$$

$$\Delta\bar{\varphi}(\bar{q}; \bar{q}_0) \equiv \Delta\hat{\varphi}(\beta_r\bar{q}, \beta_\theta\bar{q} + \beta_\theta\bar{q}_0). \quad (2.48)$$

This description is particularly useful for calculating and visualizing the SSF in later sections.

III. SCALAR SELF-FORCE PROBLEM

A. Overview

We use the same scalar model and resulting SSF formalism as outlined in our previous paper [39]. We give a brief summary here to establish notation. The small body is treated as a point particle with mass μ following an (arbitrary) geodesic about a Kerr black hole with mass M and spin a , but with the particle endowed with a scalar charge $q \sim \mu \ll M$. We neglect gravitational perturbations and the GSF due to the mass μ . The motion of the charge

sources a radiative scalar field Φ , which satisfies the curved-space Klein-Gordon equation [49]

$$g^{\alpha\beta}\nabla_\alpha\nabla_\beta\Phi = -4\pi\rho, \quad (3.1)$$

where ρ is the scalar charge density, and the covariant derivative ∇_α is taken with respect to the stationary Kerr background $g_{\alpha\beta}$. The charge density takes the form

$$\rho = q \frac{\delta(r - r_p(t))\delta(\cos\theta - \cos\theta_p(t))\delta(\varphi - \varphi_p(t))}{V_{ir}(r) + V_{i\theta}(\theta)}. \quad (3.2)$$

The scalar field produces a backreaction on the scalar charge in the form of a SSF F_α (per unit charge) that drives its motion off of a background geodesic [50],

$$u^\beta\nabla_\beta(\mu u^\alpha) = q^2 F^\alpha. \quad (3.3)$$

Unlike the gravitational case, the SSF is not orthogonal to the four-velocity and contributes to a variation in the rest mass

$$\frac{d\mu}{d\tau} = -q^2 u^\alpha F_\alpha, \quad (3.4)$$

requiring all four components of the SSF to be computed.

The contribution of Φ to the SSF can be completely encoded in the Detweiler-Whiting regular field Φ^R [50,51]

$$q^2 F^\alpha = \lim_{x^\mu \rightarrow x_p^\mu} q g^{\alpha\beta} \nabla_\beta \Phi^R. \quad (3.5)$$

The regular field $\Phi^R = \Phi^{\text{ret}} - \Phi^S$ is defined as the difference between the retarded field Φ^{ret} , which satisfies Eq. (3.1) with causal boundary conditions, and the singular field Φ^S , which also satisfies Eq. (3.1) (but with different boundary conditions) and which captures the local singular behavior.

This makes both Φ^{ret} and Φ^S divergent along the point-particle worldline, and their subtraction from one another requires a careful regularization procedure. We make use of mode-sum regularization [52,53]

$$F_\alpha = \lim_{x^\mu \rightarrow \pm x_p^\mu} \sum_{l=0}^{\infty} (F_{\alpha\pm}^{\text{ret},l} - F_{\alpha\pm}^{S,l}), \quad (3.6)$$

where $F_{\alpha\pm}^{\text{ret},l}$ and $F_{\alpha\pm}^{S,l}$ are the finite spherical harmonic moments of the full divergent quantities $q^2 F_\alpha^{\text{ret}} \equiv q \nabla_\alpha \Phi^{\text{ret}}$ and $q^2 F_\alpha^S \equiv q \nabla_\alpha \Phi^S$. The \pm notation accounts for the fact that the moments for some vector components are discontinuous at the point source, with their value depending upon the direction in r in which the limit is taken.

In the following subsections we outline how $F_\alpha^{\text{ret},l}$ and $F_\alpha^{S,l}$ are constructed for a point source following an arbitrary geodesic. We calculate the geodesic SSF, finding

⁶Our resonant angle \bar{q} differs from the resonant variable $q_\perp = \beta_\theta q_r - \beta_r q_\theta$ used by other authors (e.g., [19]).

the force along a background geodesic, and not the self-consistent SSF that would result from applying the back-reaction continuously.

B. The retarded field Φ^{ret}

In the Kerr background Eq. (3.1) is amenable to separation of variables if we both decompose Φ^{ret} in azimuthal m modes and transform to the frequency domain [49,54]. The discrete spectrum of the bound source motion reduces the frequency-domain representation of the field to a set of discrete sums

$$\Phi^{\text{ret}} = q \sum_{\hat{l}mkn} R_{\hat{l}mkn}(r) S_{\hat{l}mkn}(\theta) e^{im\varphi} e^{-i\omega_{mkn}t}, \quad (3.7)$$

where the discrete frequency spectrum ω_{mkn} is defined in Eq. (2.17), and the sum

$$\sum_{\hat{l}mkn} \equiv \sum_{\hat{l}=0}^{+\infty} \sum_{m=-\hat{l}}^{\hat{l}} \sum_{k=-\infty}^{+\infty} \sum_{n=-\infty}^{+\infty} \quad (3.8)$$

is a compact notation for the sums over \hat{l} and m and the harmonics of the polar and radial motions.

In the decomposition, $S_{\hat{l}mkn}(\theta)$ is the scalar spheroidal harmonic (spin weight 0) with spheroidicity $\sigma^2 = -a^2 \omega_{mkn}^2$, and $R_{\hat{l}mkn}(r)$ is the solution to the (scalar) radial inhomogeneous Teukolsky equation [49]. We distinguish between spheroidal and spherical harmonic indices using \hat{l} and l , respectively. In our calculations, we construct $S_{\hat{l}mkn}$ as a sum over spherical harmonics

$$S_{\hat{l}mkn}(\theta) e^{im\varphi} = \sum_{l=|m|}^{\infty} b_{\hat{l}mkn}^l Y_{lm}(\theta, \varphi), \quad (3.9)$$

where the coefficients $b_{\hat{l}mkn}^l$ satisfy a three-term recurrence relation described in [39].

C. Radial mode functions and extended homogeneous solutions

The radial mode functions $R_{\hat{l}mkn}$ are solved in a way that allows us to apply the method of extended homogeneous solutions [55–59]. This technique circumvents the appearance of Gibbs ringing in the time-domain retarded field (3.7) when the source terms are pointlike distributions. The method starts with calculating the radial mode functions in the frequency domain. We first transform to the tortoise coordinate r_* by integrating

$$\frac{dr_*}{dr} = \frac{\varpi^2}{\Delta}, \quad (3.10)$$

and then introduce scaled radial functions

$$X_{\hat{l}mkn} = \varpi R_{\hat{l}mkn}. \quad (3.11)$$

The new radial functions satisfy a radial wave equation

$$\left[\frac{d^2}{dr_*^2} - U_{\hat{l}mkn}(r) \right] X_{\hat{l}mkn}(r) = Z_{\hat{l}mkn}(r), \quad (3.12)$$

where the radial potential $U_{\hat{l}mkn}$ and source term $Z_{\hat{l}mkn}$ are defined in Sec. II C of [39] and Appendix A of this paper.

We then construct (unit-normalized) homogeneous solutions $\tilde{X}_{\hat{l}mkn}^{\pm}$ that satisfy downgoing (–) and outgoing (+) wave boundary conditions at the horizon and infinity, respectively (also referred to as the in-wave and up-wave [60]). In practice, rather than numerically constructing solutions by solving (3.12), we directly compute the homogeneous radial Teukolsky solutions $\tilde{R}_{\hat{l}mkn}^{\pm}$, using the Mano-Suzuki-Takasugi function expansions [61,62], and then obtain $\tilde{X}_{\hat{l}mkn}^{\pm}$ from (3.11).

Through variation of parameters, we calculate the normalization coefficients (or Teukolsky amplitudes) $C_{\hat{l}mkn}^{\pm}$ that relate the homogeneous and inhomogeneous solutions in the source-free regions

$$X_{\hat{l}mkn}(r < r_{\text{min}}) = C_{\hat{l}mkn}^- \tilde{X}_{\hat{l}mkn}^-(r), \quad (3.13)$$

$$X_{\hat{l}mkn}(r > r_{\text{max}}) = C_{\hat{l}mkn}^+ \tilde{X}_{\hat{l}mkn}^+(r). \quad (3.14)$$

The calculation of $C_{\hat{l}mkn}^{\pm}$ is described in Appendix A and [39]. As noted previously [11,25], varying the initial conditions of the source changes $C_{\hat{l}mkn}^{\pm}$ by a phase factor [11]

$$C_{\hat{l}mkn}^{\pm}(q_{(\alpha)0}) = e^{i\xi_{mkn}(q_{(\alpha)0})} \hat{C}_{\hat{l}mkn}^{\pm}, \quad (3.15)$$

where the set of initial conditions $q_{(\alpha)0}$ is defined in (2.43). The phase offset takes the form

$$\begin{aligned} \xi_{mkn}(q_{(\alpha)0}) \equiv & m(\Delta \hat{\varphi}(q_{r0}, q_{\theta0}) - \varphi_0) \\ & - \omega_{mkn}(\Delta \hat{t}(q_{r0}, q_{\theta0}) - t_0) - kq_{\theta0} - nq_{r0}, \end{aligned} \quad (3.16)$$

and hatted normalization constants $\hat{C}_{\hat{l}mkn}^{\pm}$ are calculated assuming the fiducial orbit. We provide a derivation of this relationship in Appendix A. Equation (3.15) also holds true for the Teukolsky amplitudes calculated for gravitational perturbations [25].

With these normalized homogeneous solutions, we define the following extended homogeneous functions

$$\phi_{\hat{l}m}^{\pm}(t, r) \equiv \sum_{\hat{l}=|m|}^{+\infty} \sum_{k=-\infty}^{+\infty} \sum_{n=-\infty}^{+\infty} \phi_{\hat{l}mkn}^{\pm}(r) e^{-i\omega_{mkn}t}, \quad (3.17)$$

$$\phi_{l\hat{m}kn}^{\pm}(r) \equiv \frac{1}{\omega} b_{l\hat{m}kn}^l C_{l\hat{m}kn}^{\pm} \tilde{X}_{l\hat{m}kn}^{\pm}(r), \quad (3.18)$$

for each spherical harmonic $Y_{lm}(\theta, \varphi)$. We refer to $\phi_{lm}^{\pm}(t, r)$ as extended homogeneous functions, not extended homogeneous solutions, since by construction there are no time domain wave equations that they satisfy (the Teukolsky equation does not separate with ordinary spherical harmonics). These functions do however have the advantage that the sums in (3.17) converge exponentially, unlike those in (3.7). Furthermore, even though the individual $\hat{l}\hat{m}kn$ modes of (3.18) are not valid solutions of the inhomogeneous Teukolsky equation in the source region $r_{\min} \leq r \leq r_{\max}$, once the full field is reconstructed in the time domain by summing over all modes, we are left with extended homogeneous solutions that provide an accurate and convergent representation of the retarded field up to the location of the point charge

$$\begin{aligned} \Phi^{\text{ret}}(t, r, \theta, \varphi) &= \Phi^{-}(t, r, \theta, \varphi) \Theta(r_p(t) - r) \\ &+ \hat{\Phi}^{+}(t, r, \theta, \varphi) \Theta(r - r_p(t)), \end{aligned} \quad (3.19)$$

$$\Phi^{\pm}(t, r, \theta, \varphi) = q \sum_{lm} \phi_{lm}^{\pm}(t, r) Y_{lm}(\theta, \varphi). \quad (3.20)$$

D. Retarded and singular contributions to the SSF

Using (3.19) and (3.20), we construct the l modes of the force $F_{\alpha\pm}^{\text{ret},l}$, along the particle worldline

$$F_{\alpha\pm}^{\text{ret},l}(\lambda) = \sum_{m=-l}^l (\mathcal{D}_{\alpha}^{lm} \phi_{lm}^{\pm})(t_p, r_p) Y_{lm}(\theta_p, \varphi_p), \quad (3.21)$$

where the coordinate positions of the particle are understood to be functions of Mino time [e.g., $t_p = t_p(\lambda)$], and the operator $\mathcal{D}_{\alpha}^{lm}$ performs the following operations on the extended homogeneous functions:

$$\mathcal{D}_t^{lm} \phi_{lm}^{\pm} \equiv \partial_t \phi_{lm}^{\pm}, \quad (3.22)$$

$$\mathcal{D}_r^{lm} \phi_{lm}^{\pm} \equiv \partial_r \phi_{lm}^{\pm}, \quad (3.23)$$

$$\begin{aligned} \mathcal{D}_{\theta}^{lm} \phi_{lm}^{\pm} &\equiv \beta_{l+3,m}^{(-3)} \phi_{l+3,m}^{\pm} + \beta_{l+1,m}^{(-1)} \phi_{l+1,m}^{\pm} \\ &+ \beta_{l-1,m}^{(+1)} \phi_{l-1,m}^{\pm} + \beta_{l-3,m}^{(+3)} \phi_{l-3,m}^{\pm}, \end{aligned} \quad (3.24)$$

$$\mathcal{D}_{\varphi}^{lm} \phi_{lm}^{\pm} \equiv im \phi_{lm}^{\pm}. \quad (3.25)$$

The coefficients $\beta_{lm}^{(\pm i)}$ are defined in Appendix A of [39]⁷ and are obtained by first applying the window function proposed

⁷A minor error exists in Eq. (A4) of [39]. The coefficients $\beta_{lm}^{(\pm 3)}$ are missing a minus sign in front of the parentheses on the righthand side of Eq. (A4).

by Warburton [59] and then reprojecting the derivatives $\partial_{\theta} Y_{lm}$ onto the Y_{lm} basis. Details of this operation can be found in [59], with a correction added in [39].

The singular contribution is obtained through a local analytic expansion in the neighborhood of the source worldline [52,53,63]

$$F_{\alpha\pm}^{S,l} = A_{\alpha}^{\pm} L + B_{\alpha} + \sum_{n=1}^{+\infty} \frac{D_{\alpha,2n}}{\prod_{k=1}^n (2L-2k)(2L+2k)}, \quad (3.26)$$

where $L \equiv l + 1/2$, and the regularization parameters $A_{\alpha\pm}$, B_{α} , and $D_{\alpha,2n}$ are independent of l but functions of r_p , θ_p , u^r , u^{θ} , \mathcal{E} , \mathcal{L}_z , and \mathcal{Q} (as well as a and M). Only $A_{\alpha\pm}$ and B_{α} are known analytically for generic bound orbits in Kerr spacetime [53], while $D_{\alpha,2}$ is known analytically for equatorial orbits in Kerr [64].

The terms with higher-order parameters $D_{\alpha,2n}$ have the useful property that their l -dependent weights vanish upon summing over all l ,

$$\sum_{l=0}^{+\infty} \left[\prod_{k=1}^n (2L-2k)(2L+2k) \right]^{-1} = 0. \quad (3.27)$$

Only $A_{\alpha\pm}$ and B_{α} are needed for convergent results, but if we neglect the $D_{\alpha,2n}$ terms upon combining Eqs. (3.6) and (3.26), F_{α} converges at a rate $\sim l^{-2}$. Each $D_{\alpha,2n}$ term reintroduced to the regularization procedure improves the convergence rate by another factor of l^{-2} . Since we truncate the sum over l modes around $l_{\max} \sim 20$, we must numerically fit for the higher-order regularization parameters to improve the convergence of the mode-sum regularization. Our fitting procedure is described in [39]. The uncertainties associated with this fitting procedure often dominate other numerical errors in the calculation. We use this to obtain uncertainty estimates for our SSF results.

IV. CONSTRUCTING THE SSF FOR RESONANT AND NONRESONANT SOURCES

A. Nonresonant sources

With a generic nonresonant orbit, the SSF is multiply periodic and never repeats over the entire interval $-\infty < \lambda < \infty$. Rather than sampling the SSF over this infinite domain in λ , we map the SSF to the angle variables introduced in Sec. II E,

$$\hat{F}_{\alpha\pm}^{\text{ret},l}(q_r, q_{\theta}) = \sum_{m=-l}^l (\mathcal{D}_{\alpha}^{lm} \hat{\phi}_{lm}^{\pm})(q_r, q_{\theta}) \hat{Y}_{lm}(q_r, q_{\theta}). \quad (4.1)$$

Note that we have placed hats on all functions that are evaluated using the fiducial geodesic solutions of (2.20)–(2.23). The evolution of φ is dependent on the motion of both r and θ , so in a slight abuse of notation we reparametrize functions to have the following meaning:

$$\hat{Y}_{lm}(q_r, q_\theta) \equiv Y_{lm}(\hat{\theta}_p(q_\theta), \Delta\hat{\varphi}(q_r, q_\theta)), \quad (4.2)$$

and

$$\begin{aligned} \hat{\phi}_{lm}^\pm(q_r, q_\theta) &\equiv \sum_{\hat{l}kn} \hat{\phi}_{\hat{l}lmkn}^\pm(q_r) e^{-i(\omega_{mkn}\Delta\hat{\tau}(q_r, q_\theta) + kq_\theta + nq_r)}, \\ \hat{\phi}_{\hat{l}lmkn}^\pm(q_r) &\equiv \hat{\omega}_p^{-1}(q_r) b_{lmkn}^l \hat{C}_{lmkn}^\pm \hat{X}_{lmkn}^\pm(\hat{r}_p(q_r)). \end{aligned} \quad (4.3)$$

Here $\hat{\omega}_p(q_r) = (\hat{r}_p^2(q_r) + a^2)^{1/2}$ and the operator \mathcal{D}_α^{lm} performs the same function as before. Because the regularization parameters only vary with respect to r_p , θ_p , u^r , and u^θ (assuming the orbital constants are fixed), the singular field can also be translated into this angle variable parametrization, ultimately providing a description of the SSF in terms of q_r and q_θ ,

$$\hat{F}_\alpha(q_r, q_\theta) = \sum_{l=0}^{\infty} (\hat{F}_{\alpha\pm}^{\text{ret},l}(q_r, q_\theta) - \hat{F}_{\alpha\pm}^{\text{S},l}(q_r, q_\theta)). \quad (4.4)$$

The angle variable parametrization maps the entire self-force history onto the finite domain of the invariant two-torus visualized in Fig. 3. The SSF, projected onto this torus, can then also be represented by the (double) Fourier series

$$\begin{aligned} F_\alpha(q_r, q_\theta) &= \sum_{k=-\infty}^{+\infty} \sum_{n=-\infty}^{+\infty} g_\alpha^{kn} e^{-i(kq_\theta + nq_r)}, \\ g_\alpha^{kn} &= \frac{1}{4\pi^2} \int_0^{2\pi} dq_r \int_0^{2\pi} dq_\theta F_\alpha(q_r, q_\theta) e^{i(kq_\theta + nq_r)}. \end{aligned} \quad (4.5)$$

By densely sampling values of q_r and q_θ over the torus at evenly-spaced points, $q_{r,i} = 2\pi i/N_r$ and $q_{\theta,j} = 2\pi j/N_\theta$ (where $N_r, N_\theta \in \mathbb{Z}$), we can construct a discrete Fourier representation of the SSF

$$\begin{aligned} F_\alpha(q_r, q_\theta) &\simeq \sum_{k=0}^{N_\theta-1} \sum_{n=0}^{N_r-1} f_\alpha^{kn} e^{-i(kq_\theta + nq_r)}, \\ f_\alpha^{kn} &= \frac{1}{N_r N_\theta} \sum_{i=0}^{N_\theta-1} \sum_{j=0}^{N_r-1} F_\alpha(q_{r,i}, q_{\theta,j}) e^{i(kq_{\theta,j} + nq_{r,i})}. \end{aligned} \quad (4.6)$$

Given N_r and N_θ that are large enough such that $\max |f_\alpha^{kn} - g_\alpha^{kn}| < \epsilon_{\text{FS}}$, where ϵ_{FS} is some predefined accuracy goal, the discrete representation will provide an accurate approximation of Eq. (4.5) [39,46]. We found that sample numbers of $N_r = N_\theta = 2^8$ were typically sufficient for constructing a discrete representation that was accurate to about $\epsilon_{\text{FS}} \sim 10^{-8} - 10^{-10}$. The discrete

Fourier series provides an efficient method for storing and interpolating SSF data.

We can easily generalize our results to geodesics with arbitrary initial conditions by applying the following shifting relation,

$$F_\alpha(q_r, q_\theta; q_{a0}) = \hat{F}_\alpha(q_r + q_{r0}, q_\theta + q_{\theta0}). \quad (4.7)$$

A proof of Eq. (4.7), which applies for both the SSF and GSF, is provided in Appendix B. While this result seems almost trivial for the nonresonant case, it surprisingly plays a role in improving the efficiency of SSF calculations for resonant orbits as well, as discussed in Sec. IV B.

B. Resonant sources

The SSF experienced by a charge following an $r\theta$ -resonant geodesic requires a different treatment. The worldline of the charge is described by (2.38)–(2.41). In contrast to the SSF for a nonresonant orbit [e.g., $\hat{F}_\alpha(q_r, q_\theta)$], we construct the resonant SSF \bar{F}_α to be a function of the single resonant angle variable \bar{q} and the initial resonant phase \bar{q}_0 [defined in Eq. (2.44)]. We describe here two methods of calculating $\bar{F}_\alpha^{\text{res}}(\bar{q}, \bar{q}_0)$: the first uses the reduced mode spectrum ω_{mN} defined in (2.36) to construct the SSF on an $\hat{l}mN$ basis, while the second uses the generic mode spectrum ω_{mkn} to construct the SSF on the $\hat{l}lmkn$ basis, just as we outlined in the previous section for nonresonant orbits. These two approaches are similar to the two approaches for calculating gravitational wave fluxes discussed in [25].

1. Constructing the resonant SSF on an $\hat{l}mN$ basis

The retarded SSF sourced by an $r\theta$ -resonant geodesic, when parametrized in terms of the resonant angle variable and resonant phase, takes the form

$$\bar{F}_{\alpha\pm}^{\text{ret},l}(\bar{q}; \bar{q}_0) = \sum_{m=-l}^l (\mathcal{D}_\alpha^{lm} \bar{\phi}_{p,lm}^\pm)(\bar{q}; \bar{q}_0) \bar{Y}_{lm}(\bar{q}; \bar{q}_0), \quad (4.8)$$

where, in contrast to Eqs. (4.2) and (4.3),

$$\bar{Y}_{lm}(\bar{q}; \bar{q}_0) \equiv Y_{lm}(\bar{\theta}_p(\bar{q}; \bar{q}_0), \Delta\bar{\varphi}(\bar{q}; \bar{q}_0) - \Delta\bar{\varphi}(0; \bar{q}_0)), \quad (4.9)$$

and

$$\begin{aligned} \bar{\phi}_{lm}^\pm(\bar{q}; \bar{q}_0) &\equiv \sum_{\hat{l}=|m|}^{+\infty} \sum_{N=-\infty}^{+\infty} \bar{\phi}_{\hat{l}lmN}^\pm(\bar{q}; \bar{q}_0) \\ &\quad \times e^{-i\omega_{mN}(\Delta\bar{\tau}(\bar{q}; \bar{q}_0) - \Delta\bar{\tau}(0; \bar{q}_0) + N\bar{q})}, \\ \bar{\phi}_{\hat{l}lmN}^\pm(\bar{q}; \bar{q}_0) &\equiv \bar{\omega}_p^{-1}(\bar{q}) b_{lmN}^l \bar{C}_{lmN}^\pm(\bar{q}_0) \bar{X}_{lmN}^\pm(\bar{r}_p(\bar{q})). \end{aligned} \quad (4.10)$$

All functions and coefficients with an overbar are evaluated using the resonant geodesic solutions described by (2.38)–(2.41). The \bar{C}_{lmN}^\pm are defined in Appendix A and vary with the resonant phase parameter \bar{q}_0 . Unlike $C_{lmkn}^\pm(\bar{q}_0)$, $\bar{C}_{lmN}^\pm(\bar{q}_0)$ is not related to the fiducial case $\bar{C}_{lmN}^\pm(0)$ by a simple phase factor. Each time we calculate the SSF for a new value of \bar{q}_0 , the source term must be integrated over a new resonant orbit. Since source integration is a computationally-intensive aspect of the SSF calculation, needing to repeat this operation is not ideal. Thus, the advantage of reduced dimensionality in the mode spectrum must be weighed against the disadvantage of repeated source integration.

2. Constructing the resonant SSF on an $\hat{l}mkn$ basis

Alternatively, we first construct the fiducial SSF $\hat{F}_\alpha(q_r, q_\theta)$ using the methods outlined in Sec. IV A. Combining (4.4) and (4.7), we can then relate the resonant SSF $\bar{F}_\alpha^{\text{res}}(\bar{q}; \bar{q}_0)$ to the fiducial result by fixing the relationship between q_r and q_θ ,

$$\bar{F}_\alpha^{\text{res}}(\bar{q}; \bar{q}_0) = \hat{F}_\alpha(\beta_r \bar{q}, \beta_\theta \bar{q} + \beta_\theta \bar{q}_0). \quad (4.11)$$

In this way, we simply construct the fiducial SSF $\hat{F}_\alpha(q_r, q_\theta)$ on an $\hat{l}mkn$ basis by relating the $\hat{l}mN$ -mode functions and constants to their $\hat{l}mkn$ -mode counterparts

$$\omega_{mN} = \omega_{m(kn)_N}, \quad (4.12)$$

$$\tilde{X}_{\hat{l}mN} = \tilde{X}_{\hat{l}m(kn)_N}, \quad b_{\hat{l}mN}^l = b_{\hat{l}m(kn)_N}^l, \quad (4.13)$$

where one must be careful to understand that $(k, n)_N$ represents the set of all k and n values that produce the same value N that satisfies $N = k\beta_\theta + n\beta_r$. Significant computational time is saved by recycling values of the homogeneous radial functions for different values of k and n , provided they share the same frequency and spheroidal mode numbers (\hat{l}, m) .

The normalization coefficients are related by a coherent sum over all k and n modes that share the same frequency (given by N)

$$\bar{C}_{\hat{l}mN}^\pm(\bar{q}_0) = \sum_{(k,n)_N} e^{i\tilde{\xi}_{mkn}(\bar{q}_0)} \hat{C}_{\hat{l}mkn}^\pm, \quad (4.14)$$

as demonstrated in Appendix A of [25] and Sec. III D of [65]. In this way, each $\bar{C}_{\hat{l}mN}^\pm(\bar{q}_0)$ is a superposition of many amplitudes $\hat{C}_{\hat{l}mkn}^\pm$ that would have been regarded as independent in the nonresonant case. In a complex square, this superposition leads to constructive or destructive interference terms in the fluxes. Note that $\tilde{\xi}_{mkn}(\bar{q}_0) \equiv \xi_{mkn}(0, 0, \beta_\theta q_{\theta 0}, 0)$. Substituting Eqs. (4.12)–(4.14) into Eqs. (4.8)–(4.10), brings them into the same

form as Eqs. (4.1)–(4.3). Unlike $\tilde{X}_{\hat{l}mkn}$, each $C_{\hat{l}mkn}$ must be calculated independently, even if they share the same frequencies and spheroidal harmonic mode numbers. Essentially, by introducing the more generic mode spectrum ω_{mkn} , we circumvent the need to repeatedly evaluate each $\hat{l}mN$ mode at different initial phases, but at the expense of summing over an additional mode number. The advantage of this approach is that, once a code has already been built to calculate the fiducial SSF for nonresonant orbits, it can be easily modified to produce the SSF for resonant sources and avoids the need to construct an entirely separate code.

3. Discrete Fourier representation of the resonant SSF

The resonant SSF is periodic with respect to \bar{q} and \bar{q}_0 , and therefore can be expressed as a multiple Fourier series. By sampling the resonant SSF on an evenly spaced two-dimensional grid in \bar{q} and \bar{q}_0 , the discrete Fourier representation of $\bar{F}_\alpha^{\text{res}}$ is

$$\bar{F}_\alpha^{\text{res}}(\bar{q}; \bar{q}_0) \simeq \sum_{K=0}^{N_0-1} \sum_{N=0}^{N_{\text{res}}-1} \bar{g}_\alpha^{KN} e^{-iN\bar{q}} e^{-iK\bar{q}_0}, \quad (4.15)$$

$$\bar{g}_\alpha^{KN} = \frac{1}{N_0 N_{\text{res}}} \sum_{j=0}^{N_0-1} \sum_{i=0}^{N_{\text{res}}-1} \bar{F}_\alpha^{\text{res}}(\bar{q}_i; \bar{q}_{0j}) e^{iN\bar{q}_i} e^{iK\bar{q}_{0j}}, \quad (4.16)$$

where $\bar{q}_i = 2\pi i/N_{\text{res}}$ and $\bar{q}_{0j} = 2\pi j/N_0$, with $N_{\text{res}}, N_0 \in \mathbb{Z}$. By comparing (4.15) with (4.6) and (4.11), we can relate \hat{f}_α^{kn} and \bar{g}_α^{KN} by

$$\bar{g}_\alpha^{KN} = \hat{f}_\alpha^{K/\beta_\theta, (N-K)/\beta_r}. \quad (4.17)$$

From this relation, we see that $\bar{g}_\alpha^{KN} = 0$ unless K is a multiple of β_θ and $N - K$ is a multiple of β_r . Thus, while the resonant angle variable and the initial resonant phase more naturally capture both the coupled nature of the radial and polar motion and the sensitivity of the source to initial conditions, this parametrization is less efficient at capturing the behavior of the self-force. For example, if one wants to calculate \hat{f}_α^{kn} for $0 \leq k < N_\theta$, $0 \leq n < N_r$, then one would need to sample $N_r \times N_\theta$ points in the $q_r - q_\theta$ domain, but $\beta_r N_r \times (\beta_\theta N_\theta + \beta_r N_r)$ points in the $\bar{q} - \bar{q}_0$ domain. This oversampling occurs because the resonant parametrization does not take full advantage of the symmetries of the orbit, which are better captured by the separation of the radial and polar motion in the $q_r - q_\theta$ angle parametrization.

C. Dissipative and conservative SSF

Irrespective of the type of orbit, the self-force can be decomposed into conservative and dissipative parts, F_α^{cons} and F_α^{diss} . These parts impact the evolution of EMRIs in different ways [8, 15, 66, 67] and computationally converge at different rates in the mode-sum regularization procedure.

The dissipative part F_α^{diss} does not require regularization and converges exponentially. The conservative part F_α^{cons} requires regularization and converges as a power law in a number of l modes.

Summarizing our previous discussion [39] of this decomposition, the split depends on both the retarded force and the advanced force F_α^{adv} , which depends on the advanced scalar field solution. The decomposition is made in terms of spherical harmonic elements, e.g., $F_\alpha^{\text{adv},l}$ and is given by

$$F_\alpha^{\text{diss}} = \sum_{l=0}^{+\infty} \frac{1}{2} (F_{\alpha\pm}^{\text{ret},l} - F_{\alpha\pm}^{\text{adv},l}), \quad (4.18)$$

$$F_\alpha^{\text{cons}} = \sum_{l=0}^{+\infty} \left\{ \frac{1}{2} (F_{\alpha\pm}^{\text{ret},l} + F_{\alpha\pm}^{\text{adv},l}) - F_{\alpha\pm}^{\text{S},l} \right\}. \quad (4.19)$$

The inconvenience of calculating the advanced scalar field solution is avoided by using symmetries of Kerr geodesics [8,15,66] (summarized also in [39]), which lead to convenient relationships between spacetime components of $F_\alpha^{\text{ret},l}$ and $F_\alpha^{\text{adv},l}$,

$$F_\alpha^{\text{adv},l}(q_r, q_\theta) = \epsilon_{(\alpha)} F_\alpha^{\text{ret},l}(2\pi - q_r, 2\pi - q_\theta), \quad (4.20)$$

where $\epsilon_{(\alpha)} = (-1, 1, 1, -1)$. Thus, F_t^{diss} , F_r^{cons} , F_θ^{cons} , and F_ϕ^{diss} are symmetric (even) functions on the $q_r - q_\theta$ two-torus, while F_t^{cons} , F_r^{diss} , F_θ^{diss} , and F_ϕ^{cons} are antisymmetric (odd). These relationships between advanced and retarded solutions have been previously discussed [58,59,68] in the context of restricted orbits but, in fact, Eq. (4.20) holds for arbitrary geodesic motion.

V. RESONANT SSF RESULTS

Using the methods outlined in the prior sections, we generated new results for the SSF on six different resonant orbits, the orbital parameters of which are listed in Table I. These calculations were made with a MATHEMATICA code first described in [39]. These calculations also made use of software from the Black Hole Perturbation Toolkit [69], specifically the KERRGEODESICS and SPINWEIGHTEDSPHEROIDALHARMONICS packages.

In generating numerical results we set $M = 1$, which is assumed for the remainder of this work. Each resonant orbit had primary spin $a = 0.9$. We focused on 1:3, 1:2, and 2:3 $r\theta$ resonances, the three resonances an EMRI is most likely to encounter during its final years of evolution when its signal falls within the LISA passband [16,17]. To pick orbital parameters (p, e, x) that produce $r\theta$ -resonant frequencies, we follow the approach of Brink, Geyer, and Hinderer [48,70]. Specified values of e and x are chosen first, and then p is numerically calculated using the root-finding method described in Sec. V E of [48]. In our

TABLE I. Summary of the resonant orbits considered in Sec. V. In all cases the primary spin is $a = 0.9$ (with $M = 1$). The real number values are truncated in the table to four significant figures for brevity.

Model	p	e	x_{inc}	$\beta_r:\beta_\theta$
$e02.13$	3.622	0.2	$\cos(\pi/4)$	1:3
$e02.12$	4.508	0.2	$\cos(\pi/4)$	1:2
$e02.23$	6.643	0.2	$\cos(\pi/4)$	2:3
$e05.13$	3.804	0.5	$\cos(\pi/4)$	1:3
$e05.12$	4.607	0.5	$\cos(\pi/4)$	1:2
$e05.23$	6.707	0.5	$\cos(\pi/4)$	2:3

work all of the orbits share the same inclination, $x = \cos(\pi/4)$, while two different eccentricities, $e = 0.2$ and $e = 0.5$, are considered. The resulting values of p (for four places) for each resonant orbit are listed in Table I.

As discussed in Sec. IV, for resonant orbits we express the SSF as a function of the resonant angle variable \bar{q} and the resonant phase parameter \bar{q}_0 , i.e., $\bar{F}_\alpha^{\text{res}}(\bar{q}; \bar{q}_0)$, or (as convenient) as a function of the more general angle variables q_r and q_θ and the initial phases q_{r0} and $q_{\theta0}$, i.e., $\hat{F}_\alpha(\beta_r \bar{q}, \beta_\theta \bar{q} + \beta_\theta \bar{q}_0) = \hat{F}_\alpha(q_r, q_\theta + q_{\theta0})$. Plotting the SSF as a function of \bar{q} , as shown in Sec. V B, highlights the periodicity of the SSF during resonances and is qualitatively representative of the Mino or coordinate time dependence of the SSF. On the other hand, plotting the SSF as a function of q_r and q_θ , as shown in Sec. V C, separates the dependence of the SSF on the radial and polar motion of the orbit. This way of depicting the SSF mirrors the parametrizations used for nonresonant orbits, as seen in [38,39]. To better analyze the impact of different orbital parameters and types of resonances, we present each spacetime component of the self-force separately.

A. Regularization and convergence of results

The SSF is constructed by mode-sum regularization and the numerical fitting procedures discussed in Sec. III D. The convergence of the mode-sum regularization procedure is well understood: subtracting the analytically known regularization parameters, A_α and B_α , produces residuals that fall off as $\sim l^{-2}$ for large l . There is no fundamental difference when an orbit is on resonance. In Fig. 4 we plot the mode-sum convergence of $\bar{F}_\phi^{\text{res}}$ at the point $(\bar{q} = 5\pi/16, \beta_\theta \bar{q}_0 = 5\pi/32)$ for all six resonant configurations. Points refer to the l -mode residuals that result from subtracting the analytically known and numerically fitted regularization parameters, while the lines depict expected power-law convergence rates for large l . In each resonance that we consider, the residuals approach their expected asymptotic rates of convergence.

While all of the models have the same asymptotic behavior at large l , Fig. 4 demonstrates that for low l modes the $e = 0.2$ sources converge faster than those with

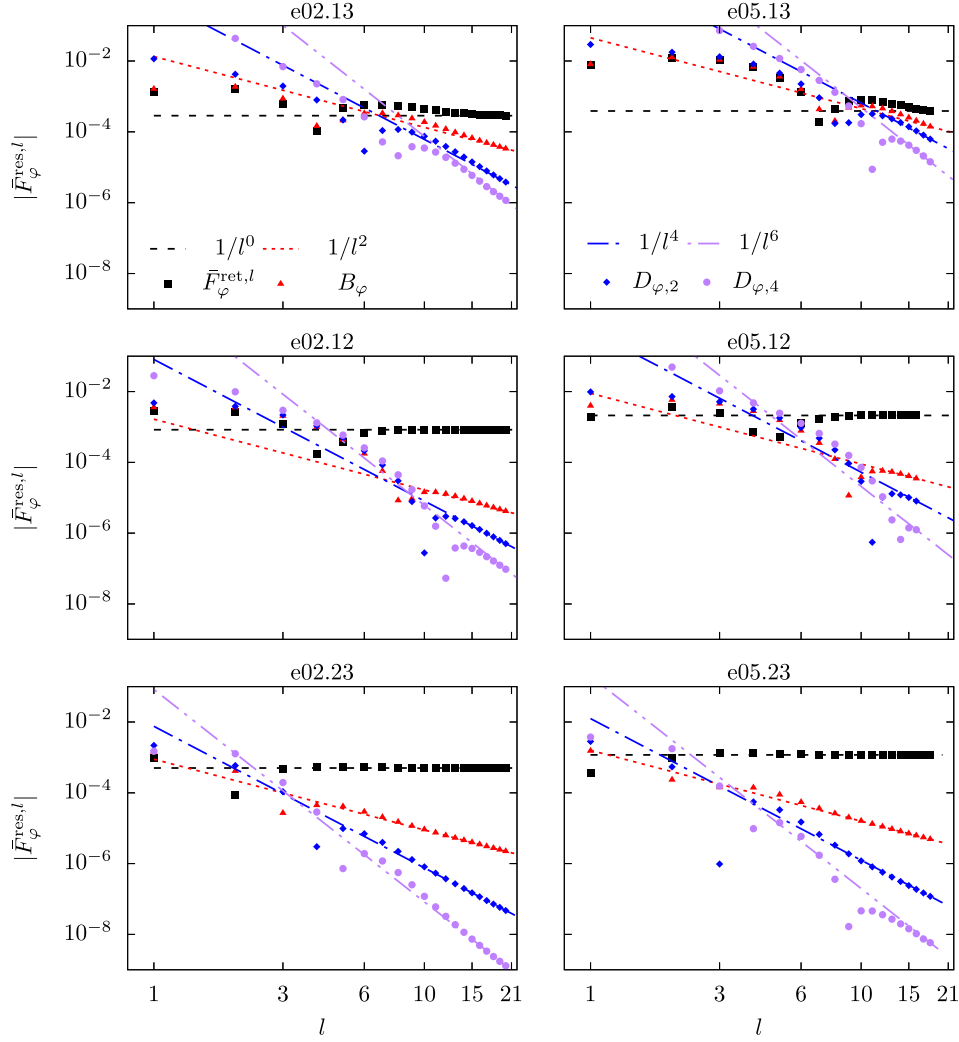


FIG. 4. Convergence of the SSF l modes for resonant models listed in Table I. The dashed and dotted lines depict comparative power-law rates of convergence for $\bar{F}_\varphi^{\text{res}}(\bar{q} = 5\pi/16; \bar{q}_0 = 5\pi/32/\beta_\theta)$ as more regularization terms are incorporated. The (black) squares represent individual l modes of the unregularized SSF, the sum of which clearly diverges. The (red) triangles are the residuals from subtracting A_φ and B_φ . The (blue) diamonds represent the residuals after subtracting $D_{\varphi,2}$, obtained through numerical fitting. The (purple) circles represent the inclusion of $D_{\varphi,4}$, also approximated via a numerical fit.

$e = 0.5$, the 2:3 resonances converge faster than the 1:2 resonances, and the 1:2 resonances converge faster than the 1:3 ones. Higher eccentricities require a broader frequency spectrum to capture the radial motion. Additionally, sources that orbit farther into the strong field excite larger perturbations and require higher frequency modes to capture the behavior of the self-force. The 1:3 resonances have the smallest pericentric separations, the 1:2 resonances have the next smallest, and the 2:3 resonances have the largest, which is reflected in varying rates of convergence at low l .

Given these factors, the $e05.13$ orbit presents the greatest challenge. For this model it takes thousands of additional modes to capture the behavior of the SSF compared to other resonant configurations. Because of the slow convergence

at low multipoles, truncating mode summations at the same value of l_{max} as the other orbits will introduce larger numerical errors in the retarded SSF contributions. While these numerical errors are still relatively small, they are significant enough that they make it much more difficult to fit for higher-order regularization parameters. The accuracy of the conservative component of the SSF suffers because of this. In consequence, the conservative SSF is only known to $\gtrsim 2$ digits of accuracy for the $e05.13$ orbit, with the numerical error greatest when a component of the SSF is in the vicinity of passing through zero. Fortunately, the dissipative component typically dominates over the conservative contribution in regions of the orbit where the conservative contribution is known less accurately.

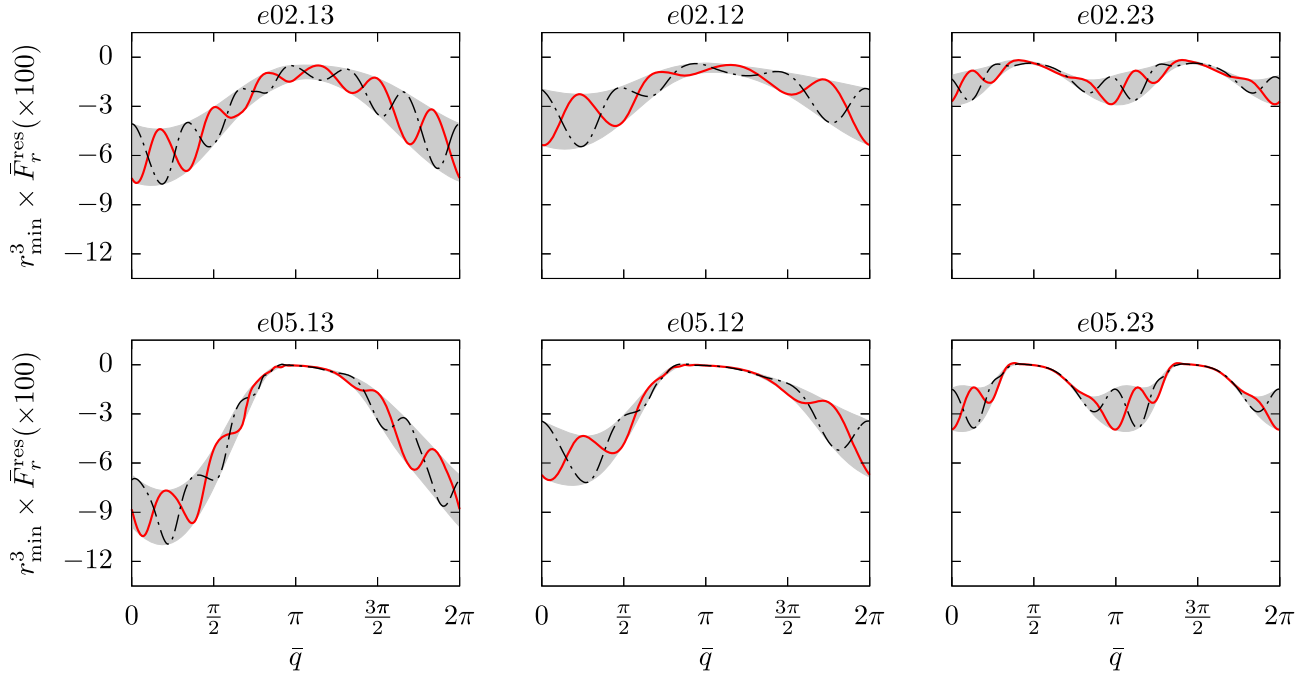


FIG. 5. Radial component of the SSF as a function of the resonant angle variable \bar{q} , i.e., $\bar{F}_r^{\text{res}}(\bar{q}; \bar{q}_0)$, for the six resonant geodesics listed in Table I. The SSF is weighted by the cube of the pericentric radius r_{min}^3 , so that all six orbits are of comparable magnitude. The dot-dashed (black) line represents the SSF for a resonant geodesic with an initial resonant phase of $\beta_\theta \bar{q}_0 = q_{\theta 0} = 0$, while the solid (red) line represents the SSF for a resonance with the same orbital parameters but an initial resonant phase of $\beta_\theta \bar{q}_0 = q_{\theta 0} = -\pi/2$. The shaded grey region represents all of the SSF values produced by varying the initial phase parameter \bar{q}_0 from 0 to 2π .

B. Scalar self-force as a function of \bar{q}

For a resonant orbit we can present the SSF in a simple line plot as a function of the net angle variable \bar{q} , as depicted in Figs. 5–8. In these plots the SSF has been weighted by the cube of the pericentric radius of the orbit (i.e., $r_{\text{min}}^3 \bar{F}_\alpha^{\text{res}}$), which more tightly bounds the variations in the SSF and facilitates comparisons across different models. Each plot shows the SSF variation with \bar{q} for two different initial conditions (i.e., values of \bar{q}_0). The dot-dashed (black) curves show the SSF when the initial polar phase is $\beta_\theta \bar{q}_0 = q_{\theta 0} = 0$ (i.e., initial conditions $x_p^\mu(\lambda = 0) = (0, r_{\text{min}}, \theta_{\text{min}}, 0)$ and $u^r(0) = u^\theta(0) = 0$), while the solid (red) curves show the SSF when $\beta_\theta \bar{q}_0 = q_{\theta 0} = -\pi/2$ (i.e., initial conditions $x_p^\mu(\lambda = 0) = (0, r_{\text{min}}, \pi/2, 0)$, $u^r(0) = 0$, and $u^\theta(0) < 0$).⁸ The shaded grey regions depict the range of SSF values that result from varying the initial phases—either $q_{\theta 0}$ or \bar{q}_0 —through their entire range.

The SSF is, of course, periodic with respect to \bar{q} , but interestingly for the 2:3 resonances \bar{F}_t^{res} , \bar{F}_r^{res} , and $\bar{F}_\phi^{\text{res}}$ are additionally periodic on the half interval $[0, \pi]$. This behavior arises in the Kerr background because the time, radial, and azimuthal components of the SSF are invariant

⁸Note that $q_{\theta 0}$ is held constant rather than \bar{q}_0 , because the same value of \bar{q}_0 will generate different initial conditions for resonances with different values of β_θ .

under parity transformations (i.e., reflections $\theta_p \rightarrow \pi - \theta_p$), while the polar component flips sign [59] (equally true of the gravitational self-force [38]). For a 2:3 resonance, the radial motion of the orbit is identical on the intervals $[0, \pi]$ and $[\pi, 2\pi]$, while the polar motion is related by the parity transformation. From this fact follows the repetition in \bar{F}_t^{res} , \bar{F}_r^{res} , and $\bar{F}_\phi^{\text{res}}$, while also giving the reflection behavior $\bar{F}_\theta^{\text{res}}(\bar{q}; \bar{q}_0) = -\bar{F}_\theta^{\text{res}}(\bar{q} + \pi; \bar{q}_0)$.

These symmetries in the geodesic motion also manifest themselves in the number of low-frequency oscillations that appear in the SSF components, particularly in the low-eccentricity orbits. Focusing on \bar{F}_r^{res} in Fig. 5, the SSF locally peaks 6 times for the e02.13 and e02.23 models and 4 times in the e02.12 case. The peaks closely align with the epochs at which each orbit passes through its polar extrema. A similar behavior is also seen for \bar{F}_t^{res} , $\bar{F}_\phi^{\text{res}}$, and the higher eccentricity models, though for $e = 0.5$ it is more difficult to identify local peaks, particularly as the orbit approaches apocenter. For $\bar{F}_\theta^{\text{res}}$ in Fig. 7, the peaks align with the passage of the source through θ_{min} , while the troughs align with its passages through $\pi - \theta_{\text{min}}$.

The degree to which the SSF varies with respect to changes in initial phase depends primarily on which component of the SSF vector we consider. The time component, \bar{F}_t^{res} (Fig. 6), displays the least effect of varying the initial conditions. The azimuthal component, $\bar{F}_\phi^{\text{res}}$ (Fig. 8), shows slightly greater variations with respect to

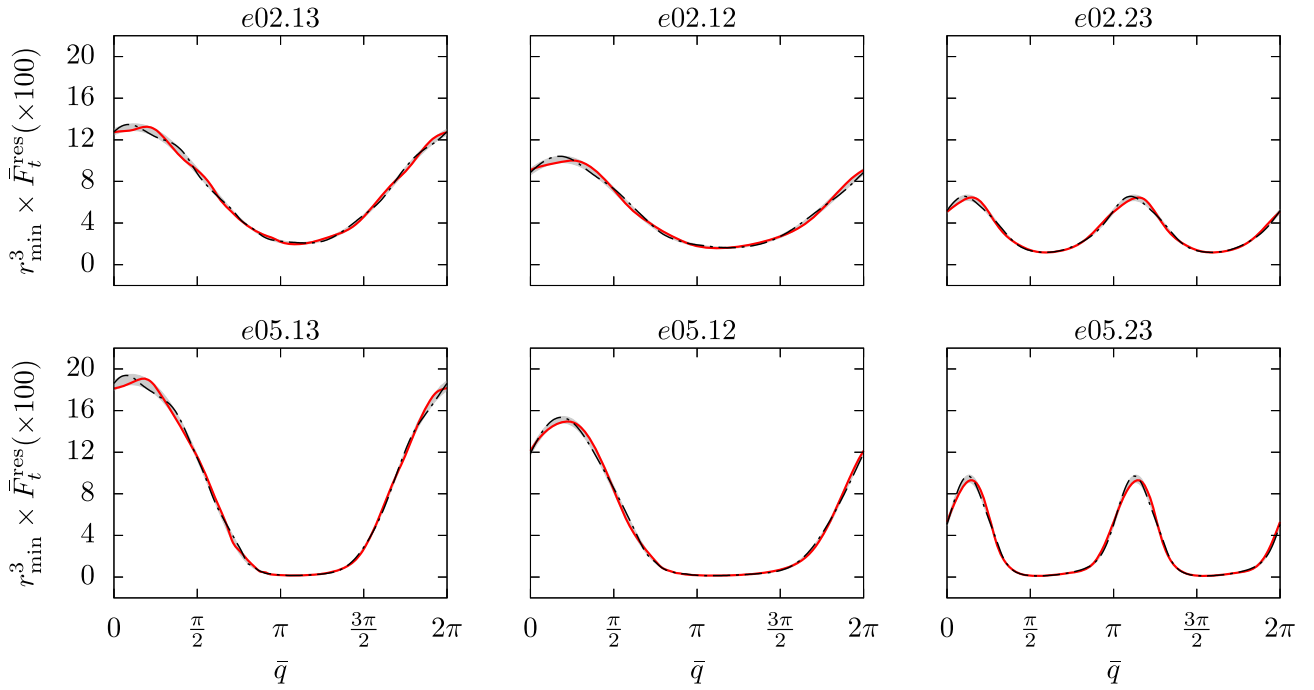


FIG. 6. Time component of the SSF as a function of the resonant angle variable \bar{q} , i.e., $\bar{F}_t^{\text{res}}(\bar{q}; \bar{q}_0)$, for the six resonant geodesics listed in Table I. The dot-dashed (black) line represents the SSF for a resonant geodesic with an initial resonant phase of $\beta_\theta \bar{q}_0 = q_{\theta 0} = 0$, the solid (red) line represents an initial resonant phase of $\beta_\theta \bar{q}_0 = q_{\theta 0} = -\pi/2$, and the shaded grey region represents all of the SSF values produced by varying \bar{q}_0 from 0 to 2π .

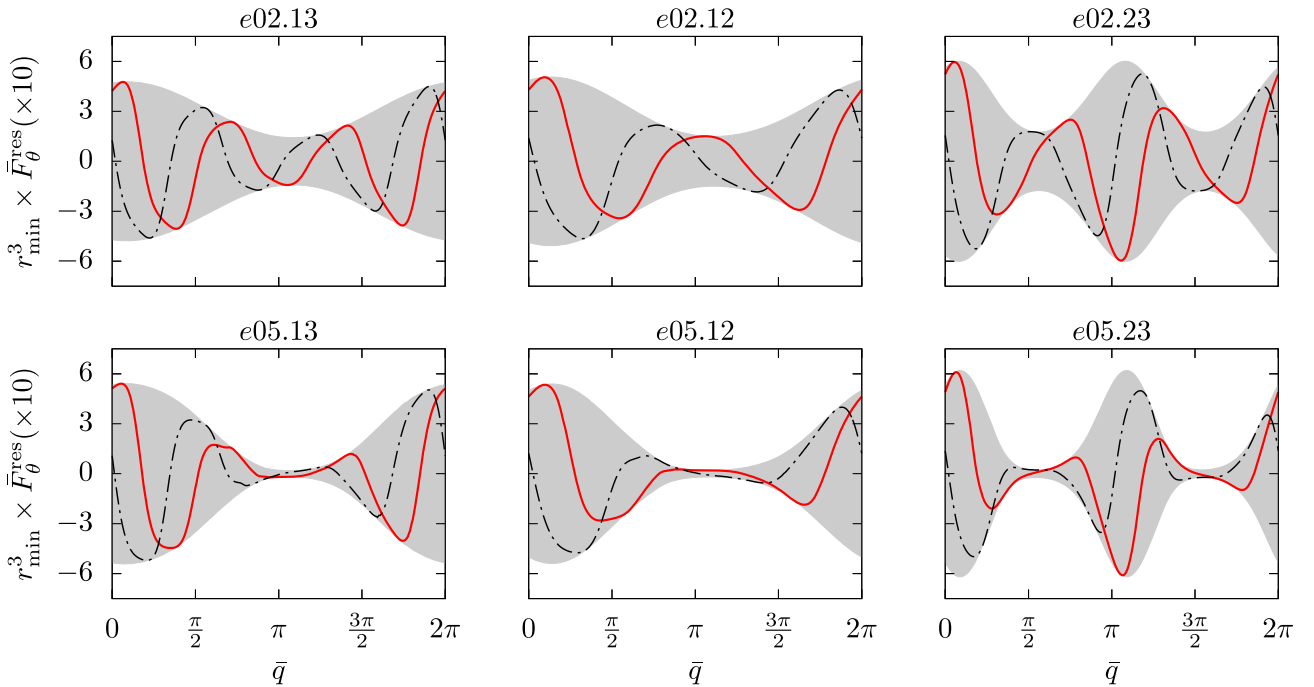


FIG. 7. Polar component of the SSF as a function of the resonant angle variable \bar{q} , i.e., $\bar{F}_\theta^{\text{res}}(\bar{q}; \bar{q}_0)$, for the six resonant geodesics listed in Table I. The dot-dashed (black) line represents the SSF for a resonant geodesic with an initial resonant phase of $\beta_\theta \bar{q}_0 = q_{\theta 0} = 0$, the solid (red) line represents an initial resonant phase of $\beta_\theta \bar{q}_0 = q_{\theta 0} = -\pi/2$, and the shaded grey region represents all of the SSF values produced by varying \bar{q}_0 from 0 to 2π .

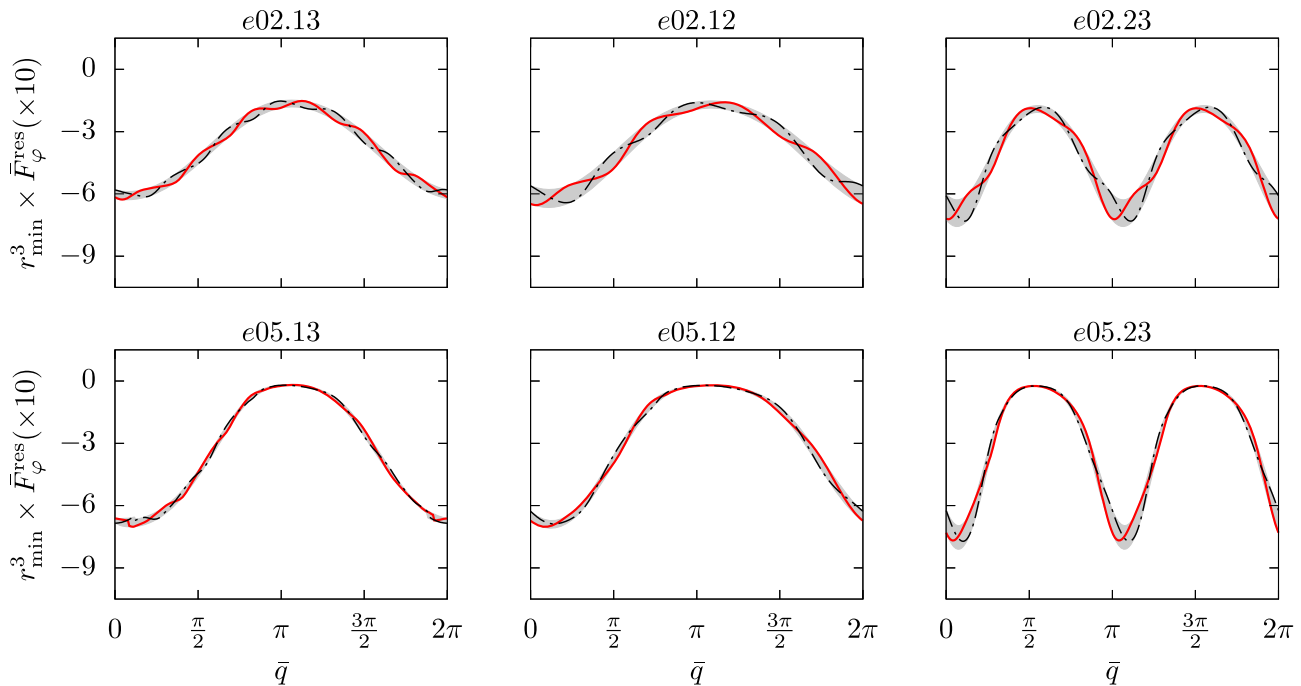


FIG. 8. Azimuthal component of the SSF as a function of the resonant angle variable \bar{q} , i.e., $\bar{F}_\varphi^{\text{res}}(\bar{q}; \bar{q}_0)$, for the six resonant geodesics listed in Table I. The dot-dashed (black) line represents the SSF for a resonant geodesic with an initial resonant phase of $\beta_\theta \bar{q}_0 = q_{\theta 0} = 0$, the solid (red) line represents an initial resonant phase of $\beta_\theta \bar{q}_0 = q_{\theta 0} = -\pi/2$, and the shaded grey region represents all of the SSF values produced by varying \bar{q}_0 from 0 to 2π .

initial conditions. The radial component, \bar{F}_r^{res} (Fig. 5), is still more affected. Finally, the polar angular component, $\bar{F}_\theta^{\text{res}}$ (Fig. 7), displays the most significant variations. To understand these variations, recall that the radial and polar position of the resonant source, \bar{r}_p and $\bar{\theta}_p$, depend on the angle variables according to

$$\bar{r}_p = \hat{r}_p(q_r) = \hat{r}(\beta_r \bar{q}), \quad (5.1)$$

$$\bar{\theta}_p = \hat{\theta}_p(q_\theta + q_{\theta 0}) = \hat{\theta}(\beta_\theta \bar{q} + \beta_\theta \bar{q}_0). \quad (5.2)$$

Consequently, a broader grey band indicates a stronger dependence on the polar motion. Thus, \bar{F}_r^{res} primarily depends on the radial motion of the source, while \bar{F}_r^{res} is sensitive to both polar and radial motions. In behavior opposite of \bar{F}_r^{res} , $\bar{F}_\theta^{\text{res}}$ is primarily dependent on the polar motion of the orbit. Finally, $\bar{F}_\varphi^{\text{res}}$ depends mostly on radial motion of the source, though the polar position becomes important near pericenter.

C. Scalar self-force as a function of q_r and q_θ

An alternative way to visualize the dependence of the SSF on the radial and polar motion of resonant orbits is to project the SSF components onto the two-torus spanned by $q_r + q_{r0}$ and $q_\theta + q_{\theta 0}$. This projection is depicted in Figs. 9–12. We again weight the SSF components by the

cube of the pericentric radius of the orbit. The dot-dashed (black) lines trace the motion of an orbit with initial conditions $\beta_\theta \bar{q}_0 = q_{\theta 0} = 0$. Sampling the SSF as the source moves along these tracks reproduces the black dot-dashed curves in Figs. 5, 6, 7, and 8. Maintaining previous notation, we refer to the SSF parametrized by $q_r + q_{r0}$ and $q_\theta + q_{\theta 0}$ as \hat{F}_α .

As observed in Sec. VB, \hat{F}_t (shown in Fig. 9) primarily depends on the radial motion, with little variation as the orbit advances along the q_θ axis. As the contours show in Figs. 10 and 12, the radial and azimuthal components, \hat{F}_r and \hat{F}_φ are sensitive to both the radial and polar motion, especially near pericenter. Finally, the contours of the SSF seen in Fig. 11 clearly demonstrate the antisymmetry across the equatorial plane of \hat{F}_θ , as discussed in the previous section.

In agreement with previous investigations [39,57–59] of the SSF, we see that \hat{F}_t is strictly positive. This contrasts with the gravitational self-force case where the time component can become negative in both radiation and Lorenz gauge [38,71].⁹ On the other hand, \hat{F}_r is predominantly negative across the entire torus, though it becomes slightly positive near apocenter. This behavior is consistent

⁹We do not try to draw any physical interpretation from this behavior since the SSF and gravitational self-force are coordinate and (in the GSF case) gauge-dependent results.

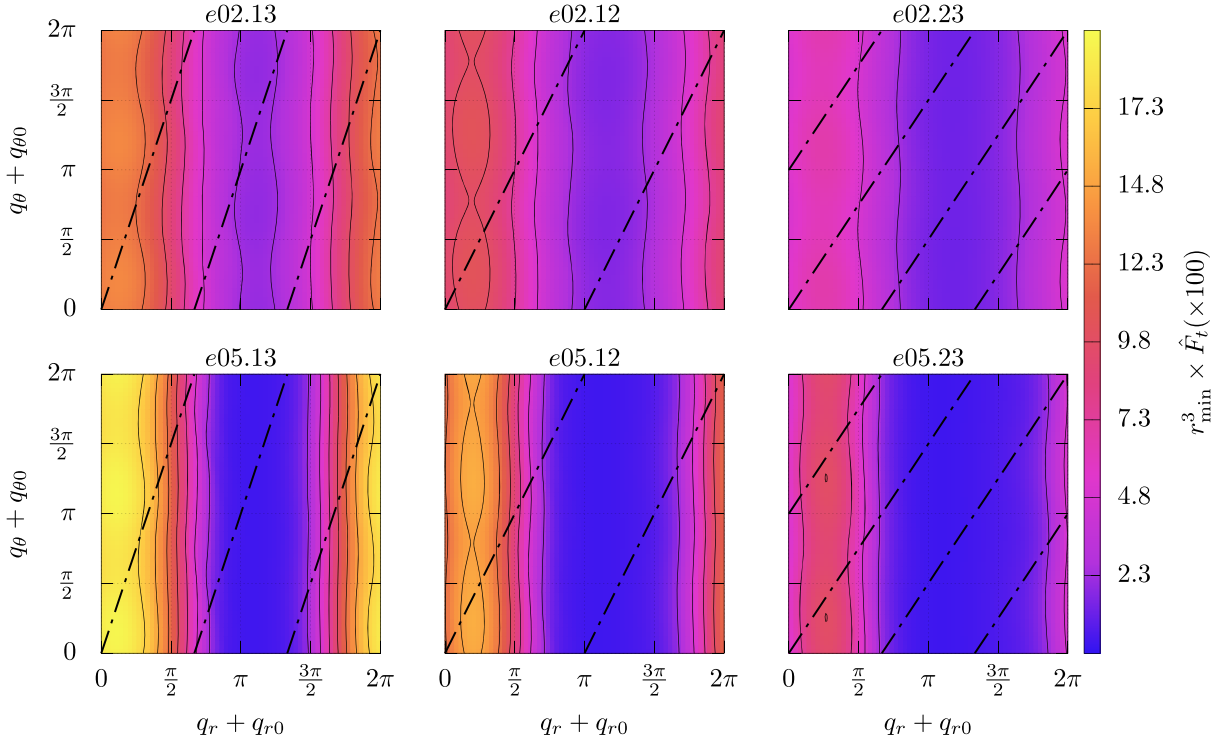


FIG. 9. Time component of the SSF \hat{F}_t projected on the poloidal motion two-torus for the six sources listed in Table I. The SSF is normalized by the cube of each source’s pericenter distance. Colors correspond to values of the self-force (see colorbar). The self-force is constant along each (solid) contour line with tic labels in the colorbar giving the values on those contours. The dot-dashed lines depict the resonant motion for fiducial initial conditions ($\bar{q}_0 = 0$).

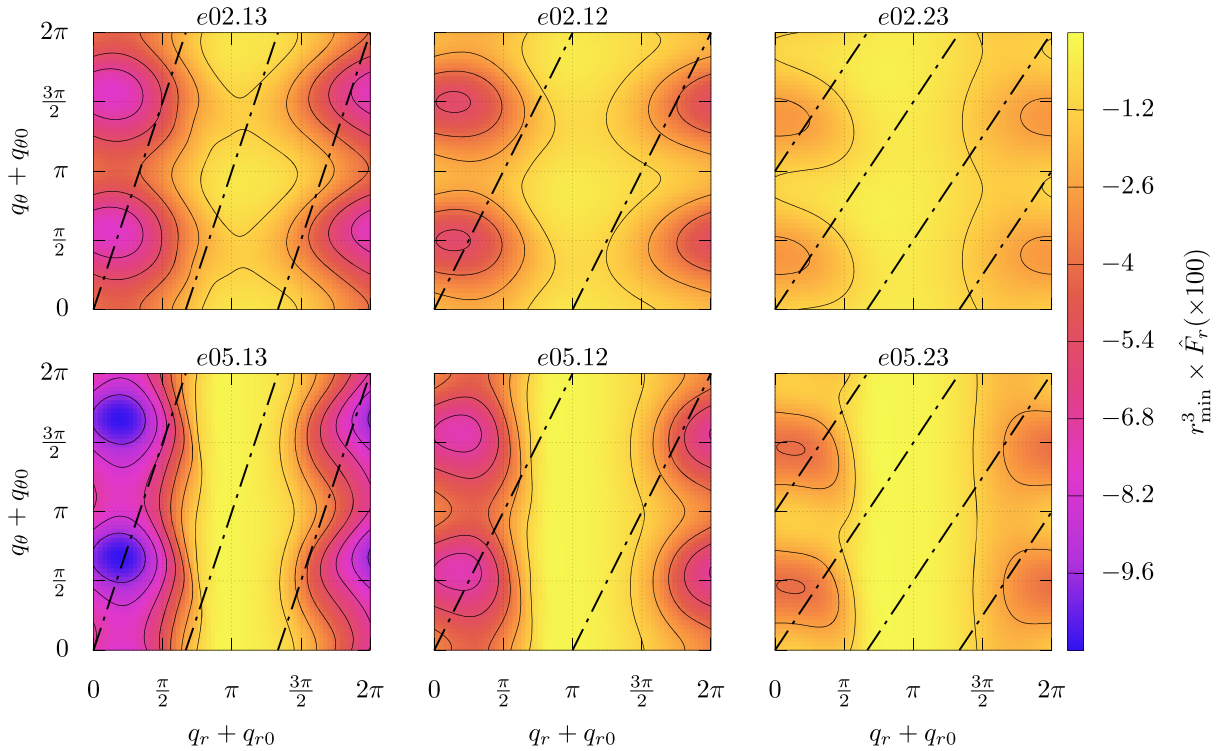


FIG. 10. Radial component of the scalar self-force \hat{F}_r for the six orbits listed in Table I.

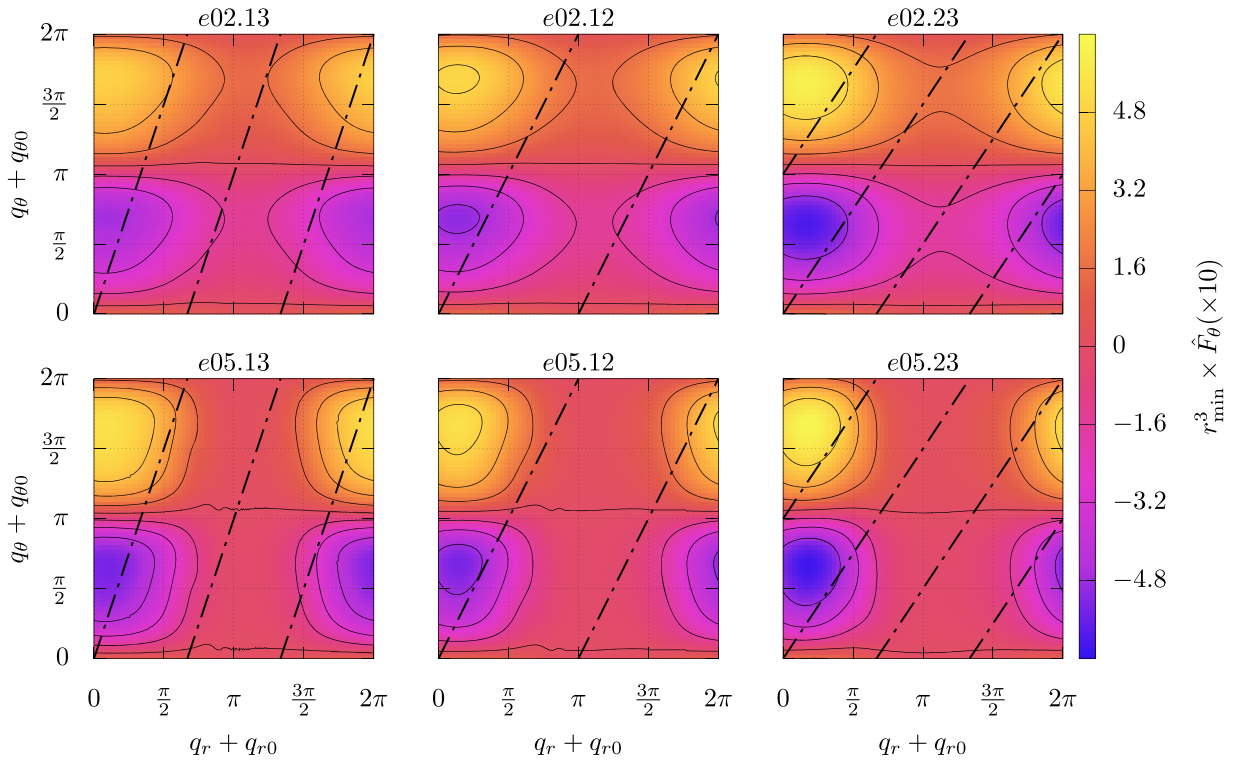


FIG. 11. Polar component of the scalar self-force \hat{F}_θ for the six orbits listed in Table I.

with the observation [57] that higher black hole spin leads to an attractive radial SSF. Large inclinations, on the other hand, lead predominantly to positive values of the SSF, as

seen in SSF results for spherical orbits [59]. However, those prior observations involved inclinations $x \gtrsim 0.5$, which we did not consider here.

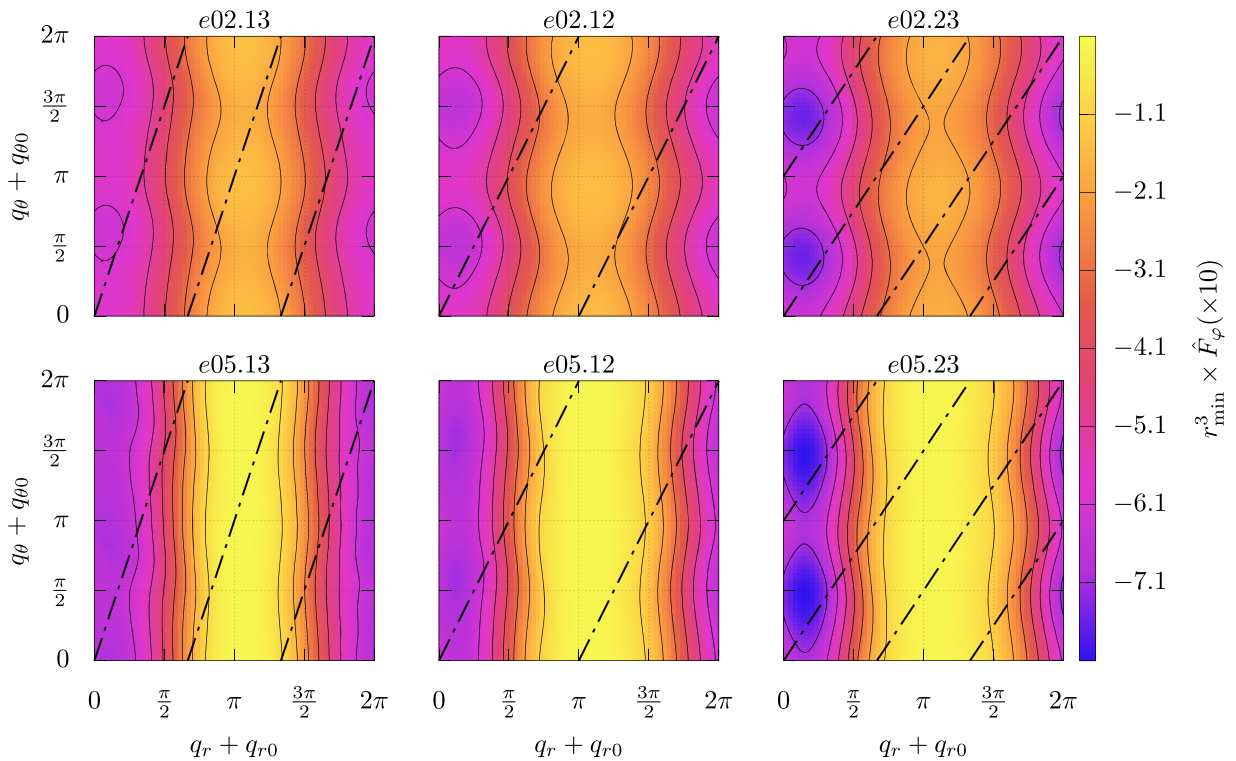


FIG. 12. Azimuthal component of the scalar self-force \hat{F}_φ for the six orbits listed in Table I.

Interestingly, while all of the SSF components peak in magnitude following pericenter passage, the magnitude of these peaks grows for \hat{F}_t and \hat{F}_r as r_{\min} decreases, while the peaks grow for \hat{F}_θ and \hat{F}_ϕ as r_{\min} increases. The latter behavior is actually due to the factor of r_{\min}^3 . If one removes this weighting, then closer pericenter passages excite larger peaks in the SSF for all components. This suggests that the leading-order behavior of \hat{F}_θ and \hat{F}_ϕ is closer to $1/r^2$, which one might expect based on dimensional analysis ($[F_{\theta,\phi}/F_{t,r}]_{\text{dim}} \sim [M]_{\text{dim}}$).

VI. EVOLUTION OF THE ORBITAL CONSTANTS

A. Overview

In the presence of radiative losses and the self-force, the ordinarily constant quantities \mathcal{E} , \mathcal{L}_z , and \mathcal{Q} are perturbed and gradually evolve according to

$$\dot{\mathcal{E}} = -\frac{q^2}{u^t} a_t, \quad \dot{\mathcal{L}}_z = \frac{q^2}{u^t} a_\phi, \quad (6.1)$$

$$\dot{\mathcal{Q}} = \frac{2}{u^t} [q^2 K_{\mu\nu} u^\mu a^\nu - (\mathcal{L}_z - a\mathcal{E})(\dot{\mathcal{L}}_z - a\dot{\mathcal{E}})], \quad (6.2)$$

where an overdot represents a derivative with respect to Boyer-Lindquist time, and the self-acceleration a^μ is given by $\mu a^\nu = (g^{\mu\nu} + u^\mu u^\nu) F_\mu = F^\nu - q^{-2} u^\nu d\mu/d\tau$. Note that the lack of orthogonality between F_ν and u^ν drives changes in the mass μ (see C 1).

The changes $\dot{\mathcal{E}}$, $\dot{\mathcal{L}}_z$, and $\dot{\mathcal{Q}}$ consist of both secularly growing and oscillating parts, with the secular piece found by orbit-averaging (6.1) and (6.2) with respect to t . For a nonresonant orbit, the averaging is over a long timescale,

$$\langle \dot{\mathcal{X}} \rangle \equiv \lim_{T \rightarrow \infty} \frac{1}{T} \int_0^T \dot{\mathcal{X}} dt, \quad \mathcal{X} = \mathcal{E}, \mathcal{L}_z, \mathcal{Q}. \quad (6.3)$$

These averages produce the leading-order adiabatic evolution of the system [15]. The time integrals can be reexpressed in terms of the angle variables that are used to parametrize the self-force. Then the averaging is done over the motion on the torus [45,65]. For nonresonant orbits, $\dot{\mathcal{E}}$, $\dot{\mathcal{L}}_z$, and $\dot{\mathcal{Q}}$ are averaged over the entire two-torus by integrating with equal weight over all q_r and q_θ . For resonances, these orbit-averages are carried out over a single one-dimensional closed track on the torus, reducing (6.3) to a single integral over the resonant phase variable \bar{q} ,

$$\mu \langle \dot{\mathcal{E}} \rangle = -\frac{q^2}{\Gamma} \int_0^{2\pi} \frac{d\bar{q}}{2\pi} \bar{\Sigma}_p \bar{F}_t^{\text{res}} = q^2 \mathcal{W}, \quad (6.4)$$

$$\mu \langle \dot{\mathcal{L}}_z \rangle = \frac{q^2}{\Gamma} \int_0^{2\pi} \frac{d\bar{q}}{2\pi} \bar{\Sigma}_p \bar{F}_\phi^{\text{res}} = q^2 \mathcal{T}, \quad (6.5)$$

$$\mu \langle \dot{\mathcal{Q}} \rangle = 2q^2 \left[-(\mathcal{L}_z - a\mathcal{E})(\dot{\mathcal{T}} - a\dot{\mathcal{W}}) + \frac{1}{\Gamma} \int_0^{2\pi} \frac{d\bar{q}}{2\pi} \bar{\Sigma}_p \bar{K}_p^{\mu\nu} \bar{u}_\mu \bar{F}_\nu^{\text{res}} \right]. \quad (6.6)$$

In the expressions above, all quantities with an overbar are understood to be functions of \bar{q} and parametrized by \bar{q}_0 [e.g., $\bar{\Sigma}_p = \bar{\Sigma}(\bar{q}; \bar{q}_0) = \bar{r}_p^2(\bar{q}) + a^2 \cos^2 \bar{\theta}_p(\bar{q} + \bar{q}_0)$]. The changes $\langle \dot{\mathcal{E}} \rangle$ and $\langle \dot{\mathcal{L}}_z \rangle$ are directly related to the average rate of work \mathcal{W} and torque \mathcal{T} done on the small body by the SSF (per charge squared) and incorporate the fact that the average change in μ vanishes (see C 1).

For nonresonant orbits the conservative components of the self-force vanish when averaged over the entire torus. This fact can be seen from the symmetries of (4.18) and (4.20), combined with the expressions for $\dot{\mathcal{E}}$, $\dot{\mathcal{L}}_z$, and $\dot{\mathcal{Q}}$. Only the dissipative self-force contributes to the leading-order adiabatic evolution of the system when it is off resonance. When on resonance, we cannot make use of these same symmetries to discard the conservative component of the self-force in (6.4), (6.5), and (6.6). However, flux-balance conditions do confirm that conservative contributions to $\langle \dot{\mathcal{E}} \rangle$ and $\langle \dot{\mathcal{L}}_z \rangle$ continue to vanish, as we further discuss in Sec. VI B. Additionally, the averages over an $r\theta$ resonance retain their dependence on \bar{q}_0 , meaning that they vary according to the initial phase at which the system enters a resonance, as demonstrated previously [17,25]. Thus different initial conditions can either diminish or enhance the averaged evolution of \mathcal{E} , \mathcal{L}_z , and \mathcal{Q} during a resonance. The following subsections detail this behavior in the scalar case and provide numerical data on how the conservative and dissipative components of the SSF contribute to $\langle \dot{\mathcal{E}} \rangle$, $\langle \dot{\mathcal{L}}_z \rangle$, and $\langle \dot{\mathcal{Q}} \rangle$.

B. Energy and angular momentum changes for a resonant orbit

Flux-balance equates the average changes in the orbital energy and angular momentum, $\langle \dot{\mathcal{E}} \rangle$ and $\langle \dot{\mathcal{L}}_z \rangle$, to the average radiative fluxes [8,60,72]. For energy, the average work \mathcal{W} done by the SSF balances the total flux $\langle \dot{\mathcal{E}} \rangle^{\text{tot}}$ radiated by the scalar field to infinity and down the horizon, with the on-resonance fluxes having slightly modified expressions

$$-\mathcal{W} = \langle \dot{\mathcal{E}} \rangle^{\text{tot}} \equiv \langle \dot{\mathcal{E}} \rangle^{\mathcal{H}} + \langle \dot{\mathcal{E}} \rangle^{\infty}, \quad (6.7)$$

$$\langle \dot{\mathcal{E}} \rangle^{\mathcal{H}} = \frac{1}{4\pi} \sum_{\ell=0}^{\infty} \sum_{m=-\ell}^{\ell} \sum_{N=-\infty}^{\infty} \omega_{mN} \gamma_{mN} |\bar{C}_{\ell m N}^-|^2, \quad (6.8)$$

$$\langle \dot{\mathcal{E}} \rangle^{\infty} = \frac{1}{4\pi} \sum_{\ell=0}^{\infty} \sum_{m=-\ell}^{\ell} \sum_{N=-\infty}^{\infty} \omega_{mN}^2 |\bar{C}_{\ell m N}^+|^2. \quad (6.9)$$

TABLE II. Energy and angular momentum fluxes for the resonant-orbit models listed in Table I. Fluxes through the horizon, $\langle \dot{E} \rangle^{\mathcal{H}}$ and $\langle \dot{L}_z \rangle^{\mathcal{H}}$, and infinity, $\langle \dot{E} \rangle^{\infty}$ and $\langle \dot{L}_z \rangle^{\infty}$, are included. Each model contains a row of fluxes for an orbit with initial phase $q_{\theta 0} = \beta_{\theta} \bar{q}_0 = 0$ and a row of fluxes for an orbit with $q_{\theta 0} = \beta_{\theta} \bar{q}_0 = -\pi/2$. A third row in each case shows the \bar{q}_0 averages of the fluxes as defined by (6.13), which ignores constructive and destructive interference terms. The reported precision in each flux indicates the accuracy of each calculation (though we truncate more accurate results at nine decimal places). The total fluxes are also compared to the local work and torque due to the SSF, \mathcal{W} and \mathcal{T} , to illustrate the (orbit-averaged) fractional errors in the flux balance relations. These errors range from $\sim 10^{-11}$ to $\sim 10^{-5}$, reflecting the numerical accuracy of our SSF results.

Model	$\beta_{\theta} \bar{q}_0$	$\langle \dot{E} \rangle^{\mathcal{H}} \times 10^5$	$\langle \dot{L}_z \rangle^{\mathcal{H}} \times 10^4$	$\langle \dot{E} \rangle^{\infty} \times 10^3$	$\langle \dot{L}_z \rangle^{\infty} \times 10^3$	$ 1 + \frac{\langle \dot{E} \rangle^{\text{tot}}}{\mathcal{W}} $	$ 1 + \frac{\langle \dot{L}_z \rangle^{\text{tot}}}{\mathcal{T}} $
e02.13	0	-4.411457095	-7.017966266	1.301535	7.677846	9×10^{-7}	8×10^{-7}
	$-\pi/2$	-4.411497781	-7.017992874	1.301534	7.677831	7×10^{-7}	6×10^{-7}
	avg	-4.411477437	-7.017979570	1.301535	7.677838
e02.12	0	-2.021123696	-3.395925026	0.5737075	4.843929	2×10^{-8}	2×10^{-8}
	$-\pi/2$	-2.021127357	-3.396083610	0.5736988	4.843824	2×10^{-8}	2×10^{-8}
	avg	-2.021125529	-3.396004318	0.5737031	4.843877
e02.23	0	-0.324830139	-0.877896699	0.134964247	1.762343845	6×10^{-9}	3×10^{-11}
	$-\pi/2$	-0.325170299	-0.877675562	0.134984611	1.762586419	6×10^{-9}	3×10^{-11}
	avg	-0.325000220	-0.877786129	0.134974429	1.762465132
e05.13	0	-0.482340196	-6.445882073	1.45739	7.28846	9×10^{-5}	8×10^{-5}
	$-\pi/2$	-0.480744834	-6.448440589	1.45724	7.28681	9×10^{-5}	8×10^{-5}
	avg	-0.481543289	-6.447161427	1.45731	7.28763
e05.12	0	-0.364726314	-2.915401042	0.590229	3.85672	3×10^{-5}	2×10^{-5}
	$-\pi/2$	-0.361475840	-2.919310921	0.589990	3.85408	3×10^{-5}	2×10^{-5}
	avg	-0.363102237	-2.917355986	0.590110	3.85540
e05.23	0	0.092800200	-0.713304108	0.12832694	1.3990094	3×10^{-7}	2×10^{-7}
	$-\pi/2$	0.090053088	-0.710893569	0.12855813	1.4017751	3×10^{-7}	2×10^{-7}
	avg	0.091426409	-0.712098512	0.12844253	1.4003923

Here $\langle \dot{E} \rangle^{\mathcal{H}}$ is the energy flux (per charge squared) through the horizon, and $\langle \dot{E} \rangle^{\infty}$ is the energy flux (per charge squared) at infinity, with $\gamma_{mN} \equiv \omega_{mN} - ma/(2Mr_+)$ being the spatial frequency of the radial modes at the horizon and $r_+ \equiv M + \sqrt{M^2 - a^2}$ denoting the radius of the outer horizon. In the resonant case, the fluxes include a single sum over the net harmonic number N of the net amplitudes \bar{C}_{lmN}^{\pm} . The net amplitudes are themselves sums (4.14) over amplitudes \hat{C}_{lmkn}^{\pm} with individual radial and polar harmonic numbers n and k . These underlying sums reflect the coherence between all harmonics of the radial and polar librations that contribute to a given N . In this way, interference terms appear in the flux that would otherwise average to zero in the off-resonance case.

In a similar way the average torque \mathcal{T} applied by the SSF balances the sum of the angular momentum flux at the horizon $\langle \dot{L}_z \rangle^{\mathcal{H}}$ and at infinity $\langle \dot{L}_z \rangle^{\infty}$,

$$-\mathcal{T} = \langle \dot{L}_z \rangle^{\text{tot}} \equiv \langle \dot{L}_z \rangle^{\mathcal{H}} + \langle \dot{L}_z \rangle^{\infty}, \quad (6.10)$$

$$\langle \dot{L}_z \rangle^{\mathcal{H}} = \frac{1}{4\pi} \sum_{\hat{l}=0}^{\infty} \sum_{m=-\hat{l}}^{\hat{l}} \sum_{N=-\infty}^{\infty} m \gamma_{mN} |\bar{C}_{lmN}^-|^2, \quad (6.11)$$

$$\langle \dot{L}_z \rangle^{\infty} = \frac{1}{4\pi} \sum_{\hat{l}=0}^{\infty} \sum_{m=-\hat{l}}^{\hat{l}} \sum_{N=-\infty}^{\infty} m \omega_{mN} |\bar{C}_{lmN}^+|^2. \quad (6.12)$$

Recall from (4.14) that the net amplitude $\bar{C}_{lmN}^{\pm} = \bar{C}_{lmN}^{\pm}(\bar{q}_0)$ is a function of \bar{q}_0 , which captures the effect on the fluxes of the phase of the resonant orbit.

In a numerical calculation the fluxes tend to converge exponentially with increasing numbers of modes and only require calculation of the matching coefficients \bar{C}_{lmN}^{\pm} , not the full SSF. The effect is that the fluxes can usually be computed to high accuracy. In Table II we report numerical values for the total fluxes (at infinity and the horizon) for two different phase parameters, $q_{\theta 0} = \beta_{\theta} \bar{q}_0 = 0$ and $-\pi/2$, and for each of the models outlined in Table I. Consistent with calculations of gravitational fluxes [73], most of the horizon fluxes are negative due to superradiant scattering (each model has primary spin of $a/M = 0.9$). As expected, orbits with smaller pericentric distances r_{min} tend to produce larger fluxes, while eccentricity has a smaller effect.

In Table II we also list the computed average over \bar{q}_0 of the resonant-orbit fluxes,

$$\langle\langle \dot{X} \rangle\rangle_{\bar{q}_0} \equiv \frac{1}{2\pi} \int_0^{2\pi} \langle \dot{X} \rangle d\bar{q}_0, \quad (6.13)$$

where $X = E, L_z$. This average over \bar{q}_0 (i.e., a double averaging) gives the flux that would be seen in a system with nearly the same orbital parameters but infinitesimally off resonance so that its motion ergodically fills the torus. It is equivalent to computing the fluxes with the normal incoherent sum of terms with $|\hat{C}_{lmkn}^\pm|^2$ over all n and k . With (6.13) giving a background average, we can define the residual variation (enhancement or diminishment) in the fluxes that arise on resonance,

$$\langle \delta \dot{X} \rangle \equiv \langle \dot{X} \rangle - \langle\langle \dot{X} \rangle\rangle_{\bar{q}_0}. \quad (6.14)$$

We plot $\langle \delta \dot{E} \rangle^{\text{tot}}$ and $\langle \delta \dot{L}_z \rangle^{\text{tot}}$ for the $e02.12$ (solid black lines), $e02.23$ (dashed red lines), and $e05.23$ (dot-dashed blue lines) orbits in Fig. 13. By comparing these figures to the values in Table II, we see that the residual variations are relatively small compared to the magnitudes of the total fluxes, but they are still greater than the $\sim 10^{-8}$ fractional error in our numerical calculations.

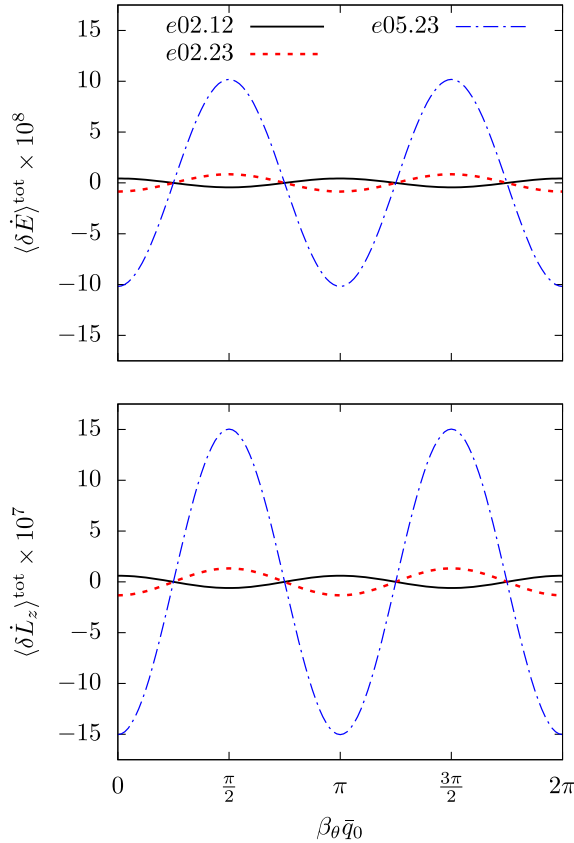


FIG. 13. Residual variations in the energy (top panel) and angular momentum (bottom panel) fluxes as a function of the initial phase $q_{00} = \beta_\theta \bar{q}_0$ for the $e02.23$ (solid black curves), $e05.23$ (dot-dashed blue curves), and $e02.12$ (dotted red curves) orbits in in Table I.

In the case of the 2:3 resonances plotted as dashed (red) and dot-dashed (blue) curves in Fig. 13, the energy and angular momentum fluxes are minimized when the motion possesses simultaneous turning points in r and θ (i.e., $\beta_\theta \bar{q}_0 = 0, \pi$). While not plotted here, the other 2:3 resonance ($e05.23$) shares this behavior. On the other hand, for the 1:2 resonance in Fig. 13, the energy and angular momentum fluxes are maximized when the motion possesses simultaneous turning points, a feature which is shared by the other 1:2- and 1:3-resonant orbits. Evidence of this behavior can also be found in Table II. Following the work of [25], we also report in Appendix D the total fractional variations $\Delta \dot{E}$ and $\Delta \dot{L}_z$ as defined by (4.5) in [25].

Additionally, we can make use of the flux-balance laws to test the accuracy of our SSF data. The fractional errors between the fluxes and the work \mathcal{W} and torque \mathcal{T} , computed via (6.7) and (6.10), are given in the last two columns of Table II. We find good agreement, with fractional errors of $\sim 10^{-11} - 10^{-5}$. Recalling the numerical convergence of the SSF displayed in Fig. 4, these fractional errors are in line with the predicted numerical accuracy of our SSF data.

The good agreement between our flux and SSF results is a further way of seeing that the conservative component of the SSF does not contribute to $\langle \dot{E} \rangle$ and $\langle \dot{L}_z \rangle$. The fluxes are *purely dissipative* quantities, and for the flux-balance laws to hold, only the dissipative component of the SSF can contribute to the averages $\langle \dot{E} \rangle$ and $\langle \dot{L}_z \rangle$, even during resonances [33].

To verify this, we calculate separately the contributions of the dissipative and conservative SSF to the residual variations $\langle \delta \dot{E} \rangle$ and $\langle \delta \dot{L}_z \rangle$ by replacing $\bar{F}_\alpha^{\text{res}}$ with $\bar{F}_\alpha^{\text{diss}}$ and $\bar{F}_\alpha^{\text{cons}}$ in (6.4) and (6.5). In Fig. 14 we plot the residual variations for the $e02.12$ (left), $e02.23$ (middle), and $e05.23$ (right) orbits. The solid (black) curves correspond to the dissipative contributions, which share the same varying behavior as seen in Fig. 13 [note the opposite sign in (6.7) and (6.10)]. The dashed (red) curves correspond to the conservative contributions, and the filled (grey) regions plot the estimated uncertainty of the conservative contributions due to truncation of the regularization procedure, which affects the conservative SSF.

The uncertainty in the conservative contributions originates in our mode-sum regularization of the SSF. As summarized in Sec. III D [and discussed with additional detail in [39], Sec. IV A, the paragraph following Eq. (4.11)], we regularize our SSF data via mode-sum regularization, but must numerically fit for higher-order regularization parameters in order to improve the numerical convergence of our l -mode sum. Without extrapolating these higher-order terms, our regularized results would be dominated by truncation errors of $O(l_{\text{max}}^{-1})$. Our extrapolation procedure typically enhances truncation error scaling

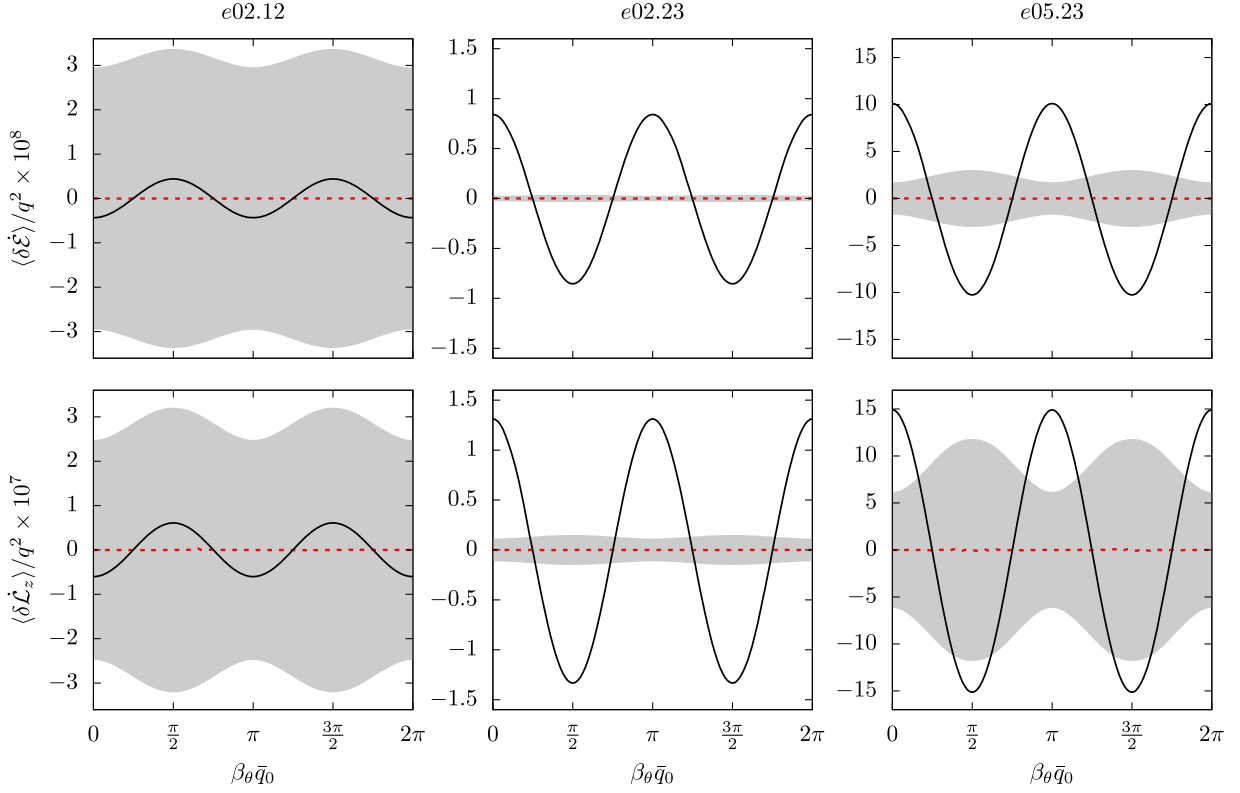


FIG. 14. Separate contributions from the dissipative and conservative components of the self-force to the residual variations $\langle \delta \dot{\mathcal{E}} \rangle$ in energy (top row) and $\langle \delta \dot{\mathcal{L}}_z \rangle$ in angular momentum (bottom row) for the $e02.12$ (left), $e02.23$ (middle), and $e05.23$ (right) orbits plotted as functions of the resonant-orbit phase. Contributions from the dissipative self-force are given by the solid (black) curves, while contributions from the conservative self-force are depicted by the dashed (red) curves. The (grey) shaded region represents the formal uncertainty in our calculation of the conservative SSF, $\langle \delta \dot{\mathcal{Q}} \rangle^{\text{cons}} \pm \sigma_{\text{cons}}$, due to fitting for higher-order regularization parameters. The calculation of σ_{cons} is discussed below (in Sec. VI B). As expected, the residual variations in energy and angular momentum arising from the conservative SSF (dashed/red curves) are consistent with zero.

to $O(l_{\text{max}}^{-7})$ but it also introduces systematic uncertainties since our extrapolated results depend on how many terms we include in our numerical fits and which multipole SSF modes we use to produce those fits. These systematic uncertainties tend to be much larger than what the improved truncation error scaling would naively suggest, and thus become the dominant form of error in our numerical conservative SSF results.¹⁰ Therefore, any quantity that depends on the conservative self-force will also have an estimated uncertainty associated with the fitting. We estimate the uncertainty of the newly calculated quantity by propagating uncertainties in additive terms, i.e.,

$$\sigma_f^2 = \left| \frac{\partial f}{\partial x_0} \right|^2 \sigma_{x_0}^2 + \left| \frac{\partial f}{\partial x_1} \right|^2 \sigma_{x_1}^2 + \dots + \left| \frac{\partial f}{\partial x_n} \right|^2 \sigma_{x_n}^2, \quad (6.15)$$

where σ_f is the propagated uncertainty of a quantity f due to its dependence on n (assumed independent) parameters

¹⁰Recall that only the conservative component of the SSF needs to be regularized.

(x_0, x_1, \dots, x_n) with (assumed uncorrelated) errors $(\sigma_{x_0}, \sigma_{x_1}, \dots, \sigma_{x_n})$. For example, $\langle \delta \dot{\mathcal{E}} \rangle^{\text{cons}}$ and its uncertainty are explicitly computed via the sums

$$\begin{aligned} \langle \delta \dot{\mathcal{E}} \rangle^{\text{cons}}(\bar{q}_0) &= \frac{q^2}{N} \sum_{n=0}^{N-1} \bar{\Sigma}_p \left(\frac{2\pi i n}{N}; \bar{q}_0 \right) \bar{F}_t^{\text{cons}} \left(\frac{2\pi i n}{N}; \bar{q}_0 \right), \\ \sigma_{\text{cons}}^2(\bar{q}_0) &= \frac{q^4}{N^2} \sum_{n=0}^{N-1} \bar{\Sigma}_p^2 \left(\frac{2\pi i n}{N}; \bar{q}_0 \right) \sigma_t^2 \left(\frac{2\pi i n}{N}; \bar{q}_0 \right), \end{aligned} \quad (6.16)$$

where $\sigma_t(\bar{q}; \bar{q}_0)$ is the estimated uncertainty of $\bar{F}_t^{\text{cons}}(\bar{q}; \bar{q}_0)$ from our fitting procedure. The first line of (6.16) is obtained by replacing the integrand of (6.4) with its discrete Fourier transform.¹¹

No uncertainty estimates for the dissipative contributions are included, as these are orders of magnitude smaller.

¹¹Recall that $\langle \langle \dot{\mathcal{E}} \rangle \rangle_{\bar{q}_0}$ vanishes exactly due to the symmetries of Kerr geodesics and, thus, $\langle \delta \dot{\mathcal{E}} \rangle^{\text{cons}} = \langle \dot{\mathcal{E}} \rangle^{\text{cons}}$.

While the conservative part leaves behind a nonzero numerical result, these variations fall well below our estimated uncertainty and are thus consistent with zero, as expected. The estimated uncertainty is much larger for the $e02.12$ model due to the slower convergence of the SSF for orbits that lie deeper in the strong field (see Fig. 4). In that model, our formal uncertainty far exceeds not only the conservative contributions but even the dissipative variations, which may point to the formal uncertainties being too conservative.

C. Carter constant and the integrability conjecture

Unlike $\langle \dot{\mathcal{E}} \rangle$ and $\langle \dot{\mathcal{L}}_z \rangle$, $\langle \dot{\mathcal{Q}} \rangle$ is not associated with a radiation flux. Instead, we must directly calculate the orbit-averaged rate of change of the Carter constant from the self-force,

$$\langle \dot{\mathcal{Q}} \rangle = \frac{1}{\Gamma} \left\langle \Sigma \frac{d\mathcal{Q}}{d\tau} \right\rangle_\lambda. \quad (6.17)$$

Here $\langle \mathcal{X} \rangle_\lambda$ refers to an average over $\mathcal{X}(\lambda)$ with respect to Mino time λ , and the proper time derivative of \mathcal{Q} is given by

$$\begin{aligned} \frac{\mu d\mathcal{Q}}{2 d\tau} &= q^2 (\csc^2 \theta \mathcal{L}_z - a\mathcal{E})(F_\varphi + a \sin^2 \theta F_t) \\ &\quad + q^2 u_\theta F_\theta - q^2 (\mathcal{L}_z - a\mathcal{E})(F_\varphi + aF_t) \\ &\quad - q^2 (\mathcal{Q} - a^2 \cos^2 \theta) u^\alpha F_\alpha, \end{aligned} \quad (6.18)$$

$$\begin{aligned} &= q^2 \Delta^{-1} (a\mathcal{L}_z - \varpi^2 \mathcal{E})(aF_\varphi + \varpi^2 F_t) \\ &\quad - q^2 \Delta u_r F_r - q^2 (\mathcal{L}_z - a\mathcal{E})(F_\varphi + aF_t) \\ &\quad - q^2 (\mathcal{Q} + r^2) u^\alpha F_\alpha. \end{aligned} \quad (6.19)$$

(See Appendix C 3.)

For nonresonant orbits, the conservative contributions to $\langle \dot{\mathcal{Q}} \rangle$ vanish due to symmetries of the motion. This can be seen by reexpressing (6.17) as a two-dimensional integral over q_r and q_θ [45,65],

$$\langle \dot{\mathcal{Q}} \rangle = \frac{1}{\Gamma} \int_0^{2\pi} \frac{dq_r}{2\pi} \int_0^{2\pi} \frac{dq_\theta}{2\pi} \left(\Sigma \frac{d\mathcal{Q}}{d\tau} \right). \quad (6.20)$$

Recall from (4.18) and (4.20) that the two components $F_{t,\varphi}^{\text{cons}}$ are antisymmetric on the $q_r - q_\theta$ torus, while the other two components $F_{r,\theta}^{\text{cons}}$ are symmetric on the torus, so that

$$F_{t,\varphi}^{\text{cons}}(2\pi - q_r, 2\pi - q_\theta) = -F_{t,\varphi}^{\text{cons}}(q_r, q_\theta), \quad (6.21)$$

$$F_{r,\theta}^{\text{cons}}(2\pi - q_r, 2\pi - q_\theta) = +F_{r,\theta}^{\text{cons}}(q_r, q_\theta). \quad (6.22)$$

Hence, if we only make use of the conservative components of the self-force in (6.18) or (6.19), then $d\mathcal{Q}^{\text{cons}}/d\tau$ is also antisymmetric. Because Σ is symmetric with respect to

the angle variables, the conservative contributions must vanish when integrated over the entire torus in (6.20). By disregarding these conservative perturbations and relating $\langle \dot{\mathcal{Q}} \rangle$ to the purely radiative (dissipative) piece of the perturbing field [8,74], (6.17) reduces to a weighted mode sum over the field's asymptotic amplitudes [11,25,74], akin to (6.7)–(6.12).

For $r\theta$ resonances, the Mino time average reduces to the single integral over \bar{q} in (6.6),

$$\langle \dot{\mathcal{Q}} \rangle = \frac{1}{\Gamma} \int_0^{2\pi} \frac{d\bar{q}}{2\pi} \left(\bar{\Sigma} \frac{d\mathcal{Q}}{d\tau} \right). \quad (6.23)$$

While the integrand in the above expression is still antisymmetric with respect to both q_r and q_θ , it is not, for a general choice of the initial resonant phase \bar{q}_0 , antisymmetric with respect to just \bar{q} (though there may be special values of \bar{q}_0 where it is). When integrated over a single closed track on the torus, (6.23) is not guaranteed to vanish, in contrast with the nonresonant case.

However, Flanagan and Hinderer [24] conjecture that dynamics driven by the conservative piece of the self-force are always integrable in Kerr spacetime¹² and cannot therefore drive secular evolution of the perturbed system through a resonance. If this integrability conjecture for conservative perturbations holds true, then $r\theta$ -resonant dynamics will be driven purely by the dissipative self-force (at adiabatic order), and $\langle \dot{\mathcal{E}} \rangle$, $\langle \dot{\mathcal{L}}_z \rangle$, and $\langle \dot{\mathcal{Q}} \rangle$ can be computed via efficient mode-sum expressions [e.g., (6.7)–(6.12)] during resonant (and nonresonant) motion, as demonstrated in [25].¹³

On the other hand, Isoyama *et al.* [32,33] also derived mode-sum expressions for $\langle \dot{\mathcal{E}} \rangle$, $\langle \dot{\mathcal{L}}_z \rangle$, and $\langle \dot{\mathcal{Q}} \rangle$ during resonances using a Hamiltonian formulation, but they found that their expression for $\langle \dot{\mathcal{Q}} \rangle$ depends on the conservative (or what they call the symmetric) component of the perturbed Hamiltonian (for the scalar case, see Eqs. (49)–(51) in [32] and for the gravitational case, see Eqs. (63) and (75) in [33]). Unless this term vanishes upon averaging, due to further symmetries, the integrability conjecture must break down during resonances, and conservative perturbations will also drive the adiabatic evolution of \mathcal{Q} .

This issue can in principle be tested using numerical modeling. To date numerical calculations of $\langle \dot{\mathcal{Q}} \rangle$ for $r\theta$ -resonant orbits [16,17,25] have not incorporated the full

¹²Conservative perturbations are integrable in Schwarzschild spacetime, but their integrability has not been fully demonstrated for Kerr [75,76].

¹³Note that the authors of [25] made no claim about the validity of the integrability conjecture, but instead adopted it as a matter of practicality since calculations of the conservative GSF were unavailable at that time (Hughes, private communications).

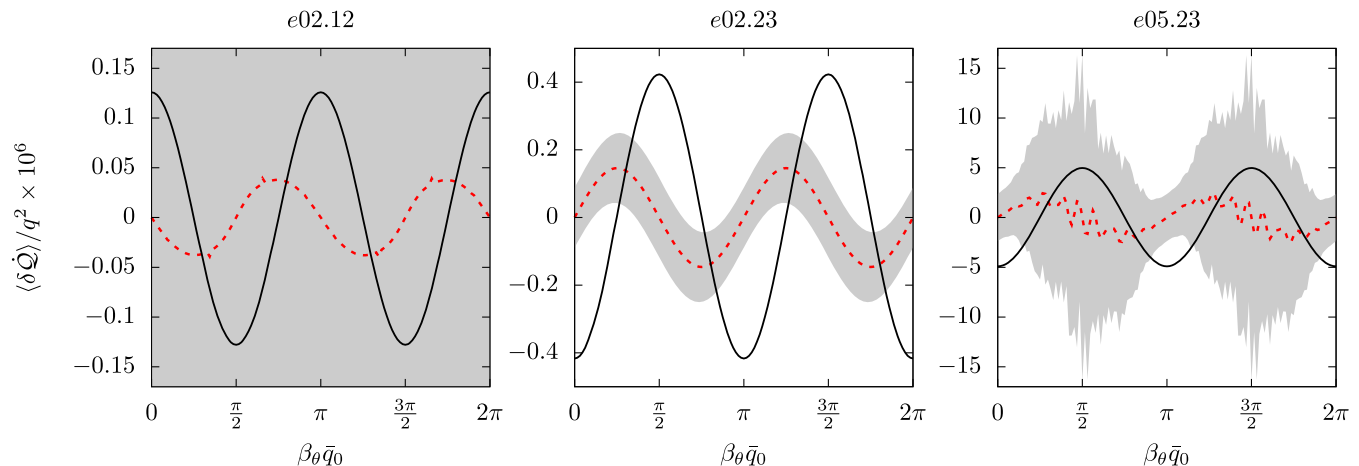


FIG. 15. Contributions from the dissipative and conservative components of the self-force to $\langle \delta \dot{Q} \rangle$ for the $e02.12$ (left), $e02.23$ (middle), and $e05.23$ (right) orbits. Contributions from the dissipative self-force are given by the solid (black) curves, while contributions from the conservative self-force are depicted by the dashed (red) curves. The (grey) shaded region represents the formal uncertainty in our calculation of the conservative SSF, $\langle \delta \dot{Q} \rangle^{\text{cons}} \pm \sigma_{\text{cons}}$, due to fitting for higher-order regularization parameters. The calculation of σ_{cons} is discussed in detail in Sec. VI B.

first-order self-force.¹⁴ Thus there is no numerical evidence to support or negate the integrability conjecture. The scalar self-force model can potentially provide some insight. We test the conjecture by measuring the relative contributions of the conservative and dissipative components of the SSF to $\langle \dot{Q} \rangle$. As we did in Sec. VI B, we replace $\bar{F}_\alpha^{\text{res}}$ in (6.6) with a breakdown in terms of $\bar{F}_\alpha^{\text{cons}}$ and $\bar{F}_\alpha^{\text{diss}}$ to calculate separately the conservative and dissipative contributions to $\langle \dot{Q} \rangle$. To compare these quantities, we then calculate their residual variations $\langle \delta \dot{Q} \rangle^{\text{cons}}$ and $\langle \delta \dot{Q} \rangle^{\text{diss}}$ as functions of the resonant-orbit phase using (6.14).

In Fig. 15, we compare the variations $\langle \delta \dot{Q} \rangle^{\text{diss}}$ (solid black curves) and $\langle \delta \dot{Q} \rangle^{\text{cons}}$ (dashed red curves) for the $e02.12$ (left), $e02.23$ (middle), and $e05.23$ (right) orbits, along with our formal uncertainty estimate σ_{cons} due to fitting for high-order regularization parameters in the conservative component of the self-force. Across all three orbits, the numerical calculation gives a smoothly varying conservative contribution to $\langle \delta \dot{Q} \rangle$. The amplitudes of the conservative contributions are slightly smaller but on the same order as the dissipative variations. The smooth variations of the conservative contributions and their comparable magnitudes to the dissipative variations strongly suggest that $\langle \dot{Q} \rangle$ does depend on conservative scalar perturbations during a resonance. However, in each case the conservative contributions from our SSF data fall

¹⁴Note that the results of Isoyama *et al.* [32,33] were purely analytical. No one has made use of the formalisms outlined in [32,33] to numerically evaluate $\langle \dot{Q} \rangle$, and our methods differ enough from the Hamiltonian formulation and Green's function methods of [32,33] that we cannot easily compare our numerical results to these works.

below or nearly within the formal uncertainty estimates. Furthermore, for all three orbits, the estimated uncertainty in our calculations of $\langle \delta \dot{Q} \rangle^{\text{cons}}$ are significantly larger than the estimated uncertainties in $\langle \delta \dot{\mathcal{E}} \rangle^{\text{cons}}$ and $\langle \delta \dot{\mathcal{L}}_z \rangle^{\text{cons}}$, as seen from comparing Figs. 14 and 15. In fact, for the $e02.12$ and $e05.23$ orbits, our estimated uncertainty is typically large enough that even if the conservative contribution dominated the variations in the dissipative contributions, they could still be consistent with zero.

In the case of the $e02.12$ model, the truncation in the regularization of the conservative part of the SSF suggests a formal uncertainty that is an order of magnitude greater than the numerically determined values of both the conservative and dissipative contributions to $\langle \delta \dot{Q} \rangle$, and the grey region engulfs the entire left panel of Fig. 15. The size of the uncertainty in this model is similar to what was seen in $\langle \delta \dot{\mathcal{E}} \rangle$ and $\langle \delta \dot{\mathcal{L}}_z \rangle$ in Fig. 14. In the $e05.23$ orbit, the calculated conservative contribution not only falls consistently below the formal uncertainty but contains high-frequency oscillations that are indicative of numerical noise. This noise appears also in the formal uncertainty estimate itself. In the $e02.23$ model, $\langle \delta \dot{Q} \rangle^{\text{cons}}$ still primarily falls within the formal uncertainty but is closest, in this case, to being a significant nonzero result. The numerical calculations, in this model at least, are close to providing evidence of the integrability conjecture's failure, but a reduction in the regularization errors by an order of magnitude or two would be required to be sure.

When compared to calculating $\langle \delta \dot{\mathcal{E}} \rangle^{\text{cons}}$ and $\langle \delta \dot{\mathcal{L}}_z \rangle^{\text{cons}}$, the estimated uncertainty proves to be much higher when analyzing the evolution of the Carter constant. In part, this is because $\langle \delta \dot{Q} \rangle^{\text{cons}}$ depends on F_θ , which tends to be the most difficult component of the SSF to accurately

extrapolate with our numerical regularization procedure. The θ component couples to even higher spheroidal modes than the other SSF components as a result of the window function described in Sec. III. If we truncate all mode calculations at a particular l_{\max} , then we can only calculate the multipoles of F_θ up to $l_{\max} - 3$, as seen from (3.21) and (3.23). Since the higher l modes are beneficial for extracting the higher-order regularization parameters, missing this higher-mode information for F_θ hampers our ability to fit for its (regularized) conservative component. We still are able to calculate F_θ to 3 or 4 significant digits, which in the absence of resonances is accurate enough to provide its contribution to EMRI evolutions that are phase accurate to less than a radian. As this analysis indicates, additional accuracy will be needed to quantify with certainty possible contributions from the conservative sector to the secular evolution of the Carter constant. In principle, we could calculate additional modes to improve the accuracy of F_θ . In practice, this is difficult because higher l modes are harder to calculate accurately due to rapid oscillatory behavior of the integrands in the source integrations. This behavior is mirrored in the gravitational case [71].

The plotted uncertainty regions in Fig. 15 provide an estimate of how well we have fit for the higher-order regularization parameters and regularized our self-force data. Any nonvanishing, and potentially smooth, variations within these uncertainty bounds could be a result of residual contributions of the singular field that were not removed during regularization. This issue is unique to averages over $r\theta$ -resonant orbit. In the nonresonant case, the singular field—much like the conservative contribution—vanishes when averaged over the entire two-torus. Even if we do not regularize the conservative component of the SSF, $\langle \delta \dot{Q} \rangle^{\text{cons}}$ will still exactly vanish for nonresonant orbits. On the other hand, averages over the singular contributions, or any antisymmetric function on the two-torus, are not guaranteed to vanish for an arbitrary $r\theta$ resonance.

We conclude that our conservative SSF results are not yet accurate enough to show a definitive conflict with the integrability conjecture. That being said, our uncertainty regions may overestimate residual contributions of the singular field that were not properly regularized. If this is the case, then the nondissipative variations that we see in Fig. 15 may very well be physical. Further tests of the integrability conjecture are necessary but will require improved regularization of the self-force. This might come from either more extensive numerical calculations and regularization parameter fitting or from the added input of analytically determined higher-order regularization parameters.

VII. SUMMARY

We considered point scalar charges following $r\theta$ -resonant geodesics in Kerr spacetime and calculated, for the first time, the resulting strong-field SSF experienced by these charges.

This work serves as a first step in understanding the still unquantified behavior of the gravitational self-force during transient orbital $r\theta$ resonances. To calculate the SSF we used a MATHEMATICA code previously developed in [39]. In constructing our SSF data, we derived a simple shifting relation, (4.11), that allows us to calculate the self-force during $r\theta$ resonances using self-force data that assumes the geodesic sources are nonresonant. This mapping provides an efficient method for analyzing the self-force as a function of the initial phase at which a system enters resonance.

When calculating the SSF, we focused on six different $r\theta$ -resonant orbits: each scalar charge followed a 1:3, 1:2, or 2:3 $r\theta$ -resonant geodesic and each orbit either had an eccentricity of 0.2 or 0.5. The full set of source parameters can be found in Table I. In Figs. 5–8, we demonstrated how varying the initial phase of $r\theta$ -resonant orbits impacts the evolution of the self-force. We then projected our SSF data onto invariant two-tori in Figs. 9–12 to display the dependence of the self-force on the radial and polar motion of the source, regardless of initial conditions and phases. We validated our SSF data by analyzing the convergence properties of our regularized self-force multipoles, as shown in Fig. 4, and by comparing the radiation fluxes to the rate of work and torque done on each scalar-charge source by the SSF via flux-balance laws, which are reported in Table II.

With these novel self-force calculations we also analyzed the impact of the conservative scalar self-force on the orbit-averaged evolution of the orbital energy $\langle \dot{E} \rangle$, z component of the angular momentum $\langle \dot{L}_z \rangle$, and Carter constant $\langle \dot{Q} \rangle$. As expected from flux-balance arguments, the contributions to $\langle \dot{E} \rangle$ and $\langle \dot{L}_z \rangle$ from the conservative SSF are negligible and consistent with zero, as shown in Fig. 14. On the other hand, our conservative SSF data substantially contribute to $\langle \dot{Q} \rangle$, as displayed in Fig. 15, though these contributions are on the order of, or much less than, our estimated uncertainty. This uncertainty is a result of the numerical regularization of the conservative SSF. Because these contributions fall within these uncertainty bounds, we cannot distinguish whether these nondissipative contributions are due to the residual singular field or the regularized conservative self-force. If these contributions are in fact from the conservative SSF, then this would indicate that the integrability conjecture proposed by Flanagan and Hinderer [24] breaks down during $r\theta$ resonances, and conservative contributions will need to be considered as predicted by Isoyama *et al.* [33]. The presence of these conservative contributions would then introduce a new numerical challenge for adiabatic calculations: to account for the evolution through resonances, adiabatic codes would need to incorporate regularization procedures to accurately quantify $\langle \dot{Q} \rangle$. Furthermore, these regularized contributions would need to be known to high levels of precision, at least to $O(\epsilon^{-1/2})$, which we have not been able to achieve with our current numerical implementations.

In future work, we will determine whether or not these nondissipative contributions to $\langle \dot{Q} \rangle$ in the scalar case are physical, or merely systematic errors, by implementing alternative improved regularization schemes and by deriving analytic expressions for the higher-order regularization parameters. If the conservative SSF contributions that we have observed are indeed physical, then we hypothesize that during $r\theta$ resonances the conservative GSF will also contribute to $\langle \dot{Q} \rangle$, as first suggested in [33]. Therefore, we are also constructing a code to calculate the GSF experienced by EMRI systems as they encounter $r\theta$ resonances to test this hypothesis.

ACKNOWLEDGMENTS

This work was supported by NSF Grants No. PHY-1806447 and No. PHY-2110335 to the University of North Carolina–Chapel Hill, and by the North Carolina Space Grant Graduate Research Fellowship. Z. N. acknowledges additional support from NSF Grant No. DMS-1439786 while in residence as a postdoctoral fellow for the Institute for Computational and Experimental Research in Mathematics in Providence, Rhode Island, during the Advances in Computational Relativity semester program. Z. N. also acknowledges support by appointment to the NASA Postdoctoral Program at the Goddard Space Flight Center, administered by Universities Space Research Association under contract with NASA.

APPENDIX A: NORMALIZATION COEFFICIENTS

We review the definitions of the normalization coefficients C_{lmkn}^{\pm} and \bar{C}_{lmN}^{\pm} and their dependence on the initial conditions of a geodesic source.

1. Nonresonant sources

We first look at nonresonant geodesic orbits and make use of the angle variables introduced in Sec. II E. The $C_{lmkn}^{\pm}(q_{(\alpha)0})$ are defined by the integrals

$$C_{lmkn}^{\pm}(q_{(\alpha)0}) = \int_{r_{\min}}^{r_{\max}} \frac{\varpi^2 \tilde{X}_{lmkn}^{\mp}(r) Z_{lmkn}(r; q_{(\alpha)0})}{W_{lmkn} \Delta(r)} dr, \quad (\text{A1})$$

where Z_{lmkn} is the radial decomposition of the source in the frequency domain

$$\rho = -\frac{\varpi^3}{4\pi \Sigma \Delta} \sum_{lmkn} Z_{lmkn}(r; q_{(\alpha)0}) S_{lmkn}(\theta) e^{im\varphi} e^{-i\omega_{mkn}t}, \quad (\text{A2})$$

and W_{lmkn} is the Wronskian

$$W_{lmkn} = \frac{\Delta}{\varpi^2} \left(\tilde{X}_{lmkn}^{-} \frac{d\tilde{X}_{lmkn}^{+}}{dr} - \tilde{X}_{lmkn}^{+} \frac{d\tilde{X}_{lmkn}^{-}}{dr} \right). \quad (\text{A3})$$

We have now explicitly included the dependence on initial conditions, which we represent with the four-tuple $q_{(\alpha)0} \equiv (t_0, q_{r0}, q_{\theta 0}, \varphi_0)$.

For the scalar point-particle source described by (3.2), Z_{lmkn} takes the form

$$Z_{lmkn}(r; q_{(\alpha)0}) = \frac{1}{4\pi^2} \int_0^{2\pi} dq_r \int_0^{2\pi} dq_{\theta} e^{i(kq_{\theta} + nq_r)} \times B_{mkn}(q_r, q_{\theta}; q_{(\alpha)0}) S_{lmkn}(\theta_p) \delta(r - r_p), \quad (\text{A4})$$

where

$$B_{mkn}(q_r, q_{\theta}; q_{(\alpha)0}) \equiv -\frac{4\pi q \Sigma_p \Delta_p}{\Gamma \varpi_p^3} \times e^{i\omega_{mkn}(\Delta t + t_0) - im(\Delta\varphi + \varphi_0)}, \quad (\text{A5})$$

$\Sigma_p = r_p^2 + a^2 \cos^2 \theta_p$, $\varpi_p^2 = r_p^2 + a^2$, $\Delta_p = \varpi_p^2 - 2Mr_p$, and the geodesic functions Δt , r_p , θ_p , and $\Delta\varphi$ are understood to be functions of q_r , q_{θ} , q_{r0} , and $q_{\theta 0}$,

$$\Delta t = \Delta \hat{t}^{(r)}(q_r + q_{r0}) - \Delta \hat{t}^{(r)}(q_{r0}) + \Delta \hat{t}^{(\theta)}(q_{\theta} + q_{\theta 0}) - \Delta \hat{t}^{(\theta)}(q_{\theta 0}), \quad (\text{A6})$$

$$r_p = \hat{r}_p(q_r + q_{r0}), \quad (\text{A7})$$

$$\theta_p = \hat{\theta}_p(q_{\theta} + q_{\theta 0}). \quad (\text{A8})$$

$$\Delta\varphi = \Delta \hat{\varphi}^{(r)}(q_r + q_{r0}) - \Delta \hat{\varphi}^{(r)}(q_{r0}) + \Delta \hat{\varphi}^{(\theta)}(q_{\theta} + q_{\theta 0}) - \Delta \hat{\varphi}^{(\theta)}(q_{\theta 0}). \quad (\text{A9})$$

(A1) then simplifies to

$$C_{lmkn}^{\pm}(q_{(\alpha)0}) = \int_0^{2\pi} \frac{dq_r}{2\pi} \int_0^{2\pi} \frac{dq_{\theta}}{2\pi} e^{i(kq_{\theta} + nq_r)} \times D_{lmkn}^{\pm}(q_r, q_{\theta}; q_{(\alpha)0}), \quad (\text{A10})$$

where

$$D_{lmkn}^{\pm}(q_r, q_{\theta}; q_{(\alpha)0}) \equiv -\frac{4\pi q}{\Gamma} \tilde{X}_{lmkn}^{\mp}(r_p) S_{lmkn}(\theta_p) \times \frac{\Sigma_p}{W_{lmkn} \varpi_p} e^{i\omega_{mkn}(\Delta t + t_0) - im(\Delta\varphi + \varphi_0)}. \quad (\text{A11})$$

(A10) separates into four one-dimensional integrals $I_{lmkn}^{(i)}$

$$C_{lmkn}^{\pm}(q_{(\alpha)0}) = I_{lmkn}^{(1)\pm}(t_0, q_{r0}) I_{lmkn}^{(2)}(q_{\theta 0}, \varphi_0) + I_{lmkn}^{(3)\pm}(t_0, q_{r0}) I_{lmkn}^{(4)}(q_{\theta 0}, \varphi_0), \quad (\text{A12})$$

where the integrals $I_{lmkn}^{(i)}$ are given in Sec. III C of [39], but with the appropriate initial parameters retained. These integrals are amenable to spectral integration techniques that provide exponentially convergent discrete representations of these integrals. These techniques are outlined in [39], and we make use of these spectral integration techniques in this work as well.

Using (A10), we can relate the normalization coefficients for an arbitrary orbit $C_{lmkn}^{\pm}(q_{(\alpha)0})$ to the coefficients for a fiducial geodesic $\hat{C}_{lmkn}^{\pm} \equiv C_{lmkn}^{\pm}(t_0 = \varphi_0 = q_{r0} = q_{\theta 0} = 0)$. Transforming to the shifted angle variables $w_r \equiv q_r + q_{r0}$ and $w_{\theta} \equiv q_{\theta} + q_{\theta 0}$, (A10) becomes

$$C_{lmkn}^{\pm}(q_{(\alpha)0}) = \int_{q_{r0}}^{2\pi+q_{r0}} \frac{dw_r}{2\pi} \int_{q_{\theta 0}}^{2\pi+q_{\theta 0}} \frac{dw_{\theta}}{2\pi} e^{i(kw_{\theta} + nw_r)} \\ \times D_{lmkn}^{\pm}(w_r - q_{r0}, w_{\theta} - q_{\theta 0}; q_{(\alpha)0}) \\ \times e^{-i(kq_{\theta 0} + nq_{r0})}.$$

Because the integrand is periodic on the intervals $q_r, q_{\theta} \in [0, 2\pi)$, we can shift the limits of integration, e.g.,

$$\int_{q_{r0}}^{2\pi+q_{r0}} \rightarrow \int_0^{2\pi} + \int_{2\pi}^{2\pi+q_{r0}} - \int_0^{q_{r0}} \rightarrow \int_0^{2\pi}.$$

Recalling (A11), we see then that D_{lmkn}^{\pm} can be rewritten as

$$D_{lmkn}^{\pm}(w_r - q_{r0}, w_{\theta} - q_{\theta 0}; q_{(\alpha)0}) \\ = e^{i\xi_{mkn}(q_{(\alpha)0})} D_{lmkn}^{\pm}(w_r, w_{\theta}; 0, 0, 0, 0), \quad (\text{A13})$$

where we have defined the phase factor ξ_{mkn} ,

$$\xi_{mkn}(q_{(\alpha)0}) \equiv -kq_{\theta 0} - nq_{r0} - \omega_{mkn}(\Delta\hat{t}^{(r)}(q_{r0}) \\ + \Delta\hat{t}^{(\theta)}(q_{\theta 0}) - t_0) \\ + m(\Delta\hat{\varphi}^{(r)}(q_{r0}) + \Delta\hat{\varphi}^{(\theta)}(q_{\theta 0}) - \varphi_0). \quad (\text{A14})$$

Combining these results, we see that different initial conditions will only alter the normalization coefficients by an overall phase,

$$C_{lmkn}^{\pm}(q_{(\alpha)0}) = e^{i\xi_{mkn}(q_{(\alpha)0})} \hat{C}_{lmkn}^{\pm}. \quad (\text{A15})$$

2. Resonant sources

We now look at $r\theta$ -resonant geodesics and make use of the resonant angle variable \bar{q} and initial resonant phase \bar{q}_0 introduced in Sec. II E. The resonant normalization constants \bar{C}_{lmN}^{\pm} are defined by the integrals

$$\bar{C}_{lmN}^{\pm}(\bar{q}_0) = \int_{r_{\min}}^{r_{\max}} \frac{\bar{\omega}^2 \bar{X}_{lmN}^{\mp}(r) \bar{Z}_{lmN}(r; \bar{q}_0)}{W_{lmN} \Delta} dr, \quad (\text{A16})$$

where \bar{Z}_{lmN} is the radial decomposition of the resonant source in the frequency domain

$$\rho = -\frac{\bar{\omega}^3}{4\pi\Sigma\Delta} \sum_{lmN} \bar{Z}_{lmN}(r; q_0) S_{lmN}(\theta) e^{im\varphi} e^{-i\omega_{mN}t},$$

and W_{lmN} is the Wronskian, defined similarly to (A3) with $\hat{lmkn} \rightarrow \hat{lmN}$. The radial dependence \bar{Z}_{lmN} takes the form

$$\bar{Z}_{lmN}(r; \bar{q}_0) = \frac{1}{2\pi} \int_0^{2\pi} d\bar{q} \bar{B}_{mN}(\bar{q}; \bar{q}_0) e^{iN\bar{q}} \\ \times S_{lmN}(\bar{\theta}_p) \delta(r - \bar{r}_p), \quad (\text{A17})$$

where

$$\bar{B}_{mN}(\bar{q}; \bar{q}_0) \equiv -\frac{4\pi q}{\Gamma} \frac{\bar{\Sigma}_p \bar{\Delta}_p}{\bar{\omega}_p^3} e^{i\omega_{mN} \Delta\bar{t} - im\Delta\bar{\varphi}}, \quad (\text{A18})$$

$\bar{\Sigma}_p = \bar{r}_p^2 + a^2 \cos^2 \bar{\theta}_p$, $\bar{\omega}^2 = \bar{r}_p^2 + a^2$, $\bar{\Delta}_p = \bar{\omega}^2 - 2M\bar{r}_p$, and the geodesic functions $\Delta\bar{t}$, \bar{r}_p , $\bar{\theta}_p$, and $\Delta\bar{\varphi}$ are understood to be functions of \bar{q} and \bar{q}_0 ,

$$\Delta\bar{t} \equiv \Delta\hat{t}^{(r)}(\bar{q}) + \Delta\hat{t}^{(\theta)}(\bar{q} + \bar{q}_0) - \Delta\hat{t}^{(\theta)}(\bar{q}_0), \quad (\text{A19})$$

$$\bar{r}_p \equiv \hat{r}_p(\bar{q}), \quad (\text{A20})$$

$$\bar{\theta}_p \equiv \hat{\theta}_p(\bar{q} + \bar{q}_0). \quad (\text{A21})$$

$$\Delta\bar{\varphi} \equiv \Delta\hat{\varphi}^{(r)}(\bar{q}) + \Delta\hat{\varphi}^{(\theta)}(\bar{q} + \bar{q}_0) - \Delta\hat{\varphi}^{(\theta)}(\bar{q}_0). \quad (\text{A22})$$

Equation (A16) simplifies to

$$\bar{C}_{lmN}^{\pm}(\bar{q}_0) = \frac{1}{2\pi} \int_0^{2\pi} d\bar{q} \bar{D}_{lmN}^{\pm}(\bar{q}; \bar{q}_0) e^{iN\bar{q}}, \quad (\text{A23})$$

where

$$\bar{D}_{lmN}^{\pm}(\bar{q}, \bar{q}_0) \equiv -\frac{4\pi q}{\Gamma} \bar{X}_{lmN}^{\mp}(\bar{r}_p) S_{lmN}(\bar{\theta}_p) \\ \times \frac{\bar{\Sigma}_p}{\bar{\omega}_p W_{lmN}} e^{i\omega_{mN} \Delta\bar{t} - im\Delta\bar{\varphi}}. \quad (\text{A24})$$

Equation (A23), like (A10) is amenable to spectral integration, though the dependence on \bar{q} and \bar{q}_0 does not separate. Each value of \bar{q}_0 (modulus 2π) leads to a unique source integral.

APPENDIX B: DEPENDENCE ON INITIAL CONDITIONS FOR THE SELF-FORCE

We derive the shifting relation (4.7) for the SSF and the GSF in outgoing radiation gauge (though we expect this derivation can be extended to other gauges as well).

1. Scalar self-force

We begin by generalizing our angle variable expression for the multipole moments of the retarded self-force given in (4.1) by retaining all dependence on initial conditions $q_{(\alpha)0}$,

$$F_{\alpha\pm}^{\text{ret},l}(q_r, q_\theta; q_{(\alpha)0}) = \sum_{m=-l}^l (D_\alpha^{lm} \phi_{lm}^\pm)(q_r, q_\theta; q_{(\alpha)0}) \times Y_{lm}(q_r, q_\theta; q_{(\alpha)0}), \quad (\text{B1})$$

where the functions Y_{lm} and ϕ_{lm}^\pm can be expressed in terms of their fiducial forms \hat{Y}_{lm} and $\hat{\phi}_{lm}^\pm$ defined in (4.2) and (4.3), respectively,

$$Y_{lm}(q_r, q_\theta; q_{(\alpha)0}) \equiv \hat{Y}_{lm}(q_r + q_{r0}, q_\theta + q_{\theta0}) \times e^{-im(\Delta\hat{\varphi}(q_{r0}, q_{\theta0}) - \varphi_0)}, \quad (\text{B2})$$

and

$$\phi_{lm}^\pm(q_r, q_\theta; q_{(\alpha)0}) \equiv \sum_{\hat{l}kn} \hat{\phi}_{\hat{l}mkn}^\pm(q_r + q_{r0}) e^{-i(kq_\theta + nq_r)} e^{-i\omega_{mkn}\Delta\hat{t}(q_r + q_{r0}, q_\theta + q_{\theta0})} e^{i\omega_{mkn}(\Delta\hat{t}(q_{r0}, q_{\theta0}) - t_0)} e^{i\xi_{mkn}(q_{(\alpha)0})}, \quad (\text{B3})$$

$$= \sum_{\hat{l}kn} \hat{\phi}_{\hat{l}mkn}^\pm(q_r + q_{r0}) e^{-i(kq_\theta + nq_r)} e^{-i(kq_{\theta0} + nq_{r0})} e^{im(\Delta\hat{\varphi}(q_{r0}, q_{\theta0}) - \varphi_0)}, \quad (\text{B4})$$

$$= \hat{\phi}_{lm}^\pm(q_r + q_{r0}, q_\theta + q_{\theta0}) e^{im(\Delta\hat{\varphi}(q_{r0}, q_{\theta0}) - \varphi_0)}, \quad (\text{B5})$$

where the exponential factor of $\xi_{mkn}(q_{(\alpha)0})$ comes from the dependence of the normalization coefficient on initial conditions in (A15).

We see that, upon combining our results for Y_{lm} and ϕ_{lm}^\pm , the exponential dependence on the initial conditions will cancel, leaving us with the shifting relation

$$F_{\alpha\pm}^{\text{ret},l}(q_r, q_\theta; q_0^\mu) = \hat{F}_{\alpha\pm}^{\text{ret},l}(q_r + q_{r0}, q_\theta + q_{\theta0}). \quad (\text{B6})$$

The same result also holds true for $F_\alpha^{S,l}$. The singular contributions along the particle worldline are only functions of r_p , θ_p , u^r , and u^θ , and all of these functions are related to their fiducial counterparts via

$$r_p(q_r; q_{r0}) = \hat{r}_p(q_r + q_{r0}), \quad (\text{B7})$$

$$\theta_p(q_\theta; q_{\theta0}) = \hat{\theta}_p(q_\theta + q_{\theta0}), \quad (\text{B8})$$

$$u^r(q_r, q_\theta; q_{r0}, q_{\theta0}) = \hat{u}^r(q_r + q_{r0}, q_\theta + q_{\theta0}), \quad (\text{B9})$$

$$u^\theta(q_r, q_\theta; q_{r0}, q_{\theta0}) = \hat{u}^\theta(q_r + q_{r0}, q_\theta + q_{\theta0}). \quad (\text{B10})$$

Consequently, (B6) also holds true for the regularized SSF F_α .

2. Gravitational self-force

Using the results presented by van de Meent in his calculation of the GSF [38], we find that (B6) also extends to the gravitational case, at least for the form of the GSF in the outgoing radiation gauge (ORG) presented in [38]. The unregularized l -mode contributions to the GSF in the ORG can be written in the form (see (44) in [38])¹⁵

$$\begin{aligned} F_{\text{Rad}}^{\mu,l\pm}(q_r, q_\theta; q_{(\alpha)0}) &= \sum_{\substack{mkn\text{si}j \\ l_1 l_2 l}} C_{mkn\text{si}j}^\mu(\hat{r}_p(q_r + q_{r0}), \hat{\theta}_p(q_\theta + q_{\theta0})) \Psi_{lmkn}^\pm(q_{r0}, q_{\theta0}) \\ &\times {}_2R_{lmkn}^{\pm,(i)}(\hat{r}_p(q_r + q_{r0})) {}_2b_{lmkn}^{l_1} {}^m A_{l_1 m}^{l_2 j} \mathcal{B}_{l_2}^l Y_{lm}(\hat{\theta}_p(q_\theta + q_{\theta0}), 0) e^{im\Delta\hat{\varphi}^{(r)}(q_r + q_{r0})} e^{im\Delta\hat{\varphi}^{(\theta)}(q_\theta + q_{\theta0})} \\ &\times e^{-i\omega_{mkn}\Delta\hat{t}^{(r)}(q_r + q_{r0})} e^{-i\omega_{mkn}\Delta\hat{t}^{(\theta)}(q_\theta + q_{\theta0})} e^{-ik(q_\theta + q_{\theta0})} e^{-in(q_r + q_{r0})} e^{-i\xi_{mkn}(q_{(\alpha)0})} + \text{c.c.}, \end{aligned} \quad (\text{B11})$$

¹⁵Our expression slightly differs from (44) of [38], which is missing a factor of Y_{lm} . In our expression, we also reformatted indices to more closely reflect the notation used in our SSF calculations.

where the functions and coefficients are defined in [38] and c.c. denotes complex conjugation of the previous terms.

As van de Meent and Shah demonstrated in [77], the asymptotic amplitudes of the ORG Hertz potential $\Psi_{lmkn}^{\pm}(q_{r0}, q_{\theta0})$ are proportional to the normalization coefficients for a gravitational source, also known as Teukolsky amplitudes, $Z_{lmkn}^{\pm}(q_{r0}, q_{\theta0})$. The Teukolsky amplitudes are also related to their fiducial forms via (A15) [25]. Consequently, the ξ_{mkn} phase in the third line of (B11) will cancel with the phase dependence that arises from $\Psi_{lmkn}^{\pm}(q_{r0}, q_{\theta0}) = e^{i\xi_{mkn}} \hat{\Psi}_{lmkn}^{\pm}$. The GSF in the ORG can then be expressed in terms of the fiducial GSF $\hat{F}_{\text{Rad}}^{\mu, l\pm}(q_r, q_{\theta}) \equiv F_{\text{Rad}}^{\mu, l\pm}(q_r, q_{\theta}; t_0 = q_{r0} = q_{\theta0} = \varphi_0 = 0)$ through the shifting relation

$$F_{\text{Rad}}^{\mu, l\pm}(q_r, q_{\theta}; q_{r0}, q_{\theta0}) = \hat{F}_{\text{Rad}}^{\mu, l\pm}(q_r + q_{r0}, q_{\theta} + q_{\theta0}). \quad (\text{B12})$$

APPENDIX C: EVOLUTION OF THE ORBITAL PARAMETERS

For completeness, we provide derivations of the orbit-averaged time derivatives of the orbital parameters μ , \mathcal{E} , \mathcal{L}_z , and \mathcal{Q} due to perturbations from the SSF. Similar derivations can be found in [11,25].

1. Rest mass

Recall that the SSF is not purely orthogonal to the four-velocity and thus contributes to the evolution of the particle's rest mass during its evolution,

$$\frac{d\mu}{d\tau} = -q^2 u^{\alpha} F_{\alpha}. \quad (\text{C1})$$

Because $q^2 F_{\alpha} = q \nabla_{\alpha} \Phi^{\text{R}}$, we can directly integrate (C1),

$$\mu(\tau) = \mu_0 - q \Phi^{\text{R}}(x_p^{\mu}(\tau)), \quad (\text{C2})$$

where the integration constant μ_0 is commonly referred to as the *bare mass*. Note that the second term is of $O(q^2/M)$ so that μ/M is constant at leading order in q/M . After a full orbital period, the value of the regular field will return to itself. Thus, via the second fundamental theorem of calculus, the orbit average of the time derivative of the rest mass vanishes,

$$\langle \dot{\mu} \rangle = 0, \quad (\text{C3})$$

where $\dot{x} \equiv dx/dt$ and the angle-bracket averages are defined in (6.3).

2. Orbital energy and angular momentum

In Kerr spacetime, orbital quantities are typically calculated with respect to Mino time λ , rather than coordinate

time t . Therefore, we reexpress the orbit-averaged time derivative of the orbital energy $\langle \dot{\mathcal{E}} \rangle$ as an average over Mino time λ [11,45]

$$\langle \dot{\mathcal{E}} \rangle = \frac{1}{\Gamma} \left\langle \frac{d\mathcal{E}}{d\lambda} \right\rangle_{\lambda} = \frac{1}{\Gamma} \left\langle \Sigma \frac{d\mathcal{E}}{d\tau} \right\rangle_{\lambda}, \quad (\text{C4})$$

where $\langle \mathcal{X} \rangle_{\lambda}$ refers to an orbit average of the quantity $\mathcal{X}(\lambda)$ with respect to λ . The right-hand side of (C4) can be further expanded by taking the proper-time derivative of (2.2),

$$\frac{d\mathcal{E}}{d\tau} = u^{\alpha} \nabla_{\alpha} (g_{\mu\nu} \xi_{(t)}^{\mu} u^{\nu}), \quad (\text{C5})$$

$$= g_{\mu\nu} (u^{\nu} u^{\alpha} \nabla_{\alpha} \xi_{(t)}^{\mu} + \xi_{(t)}^{\mu} u^{\alpha} \nabla_{\alpha} u^{\nu}), \quad (\text{C6})$$

$$= g_{\mu\nu} \xi_{(t)}^{\mu} u^{\alpha} \nabla_{\alpha} u^{\nu}, \quad (\text{C7})$$

where $u^{\nu} u^{\alpha} \nabla_{\alpha} \xi_{(t)}^{\mu}$ vanishes due to $\xi_{(t)}^{\mu}$ satisfying Killing's equation. Defining the four-acceleration a^{μ} and perpendicular self-force f^{μ} ,

$$f^{\mu} = \mu a^{\mu} \equiv (g^{\mu\nu} + u^{\mu} u^{\nu}) F_{\nu}, \quad (\text{C8})$$

(C5) then takes the compact form

$$\mu \frac{d\mathcal{E}}{d\tau} = -q^2 f_t. \quad (\text{C9})$$

Combining (C9) and (C4), we find that

$$\mu \langle \dot{\mathcal{E}} \rangle = -\frac{q^2}{\Gamma} \langle \Sigma f_t \rangle_{\lambda}, \quad (\text{C10})$$

$$= -\frac{q^2}{\Gamma} \langle \Sigma F_t \rangle_{\lambda}, \quad (\text{C11})$$

where in the second line, we have taken into account that

$$\langle \Sigma f_t \rangle_{\lambda} = \langle \Sigma (F_t + u_t u^{\alpha} F_{\alpha}) \rangle_{\lambda}, \quad (\text{C12})$$

$$= \langle \Sigma F_t \rangle_{\lambda} + q^{-2} \mathcal{E} \left\langle \frac{d\mu}{d\lambda} \right\rangle_{\lambda}, \quad (\text{C13})$$

$$= \langle \Sigma F_t \rangle_{\lambda}. \quad (\text{C14})$$

The orbit-averaged rate of change of the z component of the orbital angular momentum $\langle \dot{\mathcal{L}}_z \rangle$ can be derived in a similar manner,

$$\mu \langle \dot{\mathcal{L}}_z \rangle = \frac{q^2}{\Gamma} \langle \Sigma F_{\phi} \rangle_{\lambda}. \quad (\text{C15})$$

3. Carter constant

The orbit-averaged rate of change of the Carter constant $\langle \dot{Q} \rangle$ can be derived using the process outlined in the previous section C 2. Like $\langle \dot{\mathcal{E}} \rangle$ and $\langle \dot{L}_z \rangle$, $\langle \dot{Q} \rangle$ can be reexpressed in terms of an average over λ ,

$$\mu \langle \dot{Q} \rangle = \frac{\mu}{\Gamma} \left\langle \Sigma \frac{dQ}{d\tau} \right\rangle_{\lambda}. \quad (\text{C16})$$

Once again we can expand the right-hand side by taking the proper time derivative of the Carter constant as defined by (2.4),

$$\begin{aligned} \frac{dQ}{d\tau} &= \mu u^\mu u^\nu u^\alpha \nabla_\alpha K_{\mu\nu} + 2u^\mu K_{\mu\nu} u^\alpha \nabla_\alpha u^\nu \\ &\quad - 2(\mathcal{L}_z - a\mathcal{E}) \left(\frac{d\mathcal{L}_z}{d\tau} - a \frac{d\mathcal{E}}{d\tau} \right), \end{aligned} \quad (\text{C17})$$

which, after utilizing the properties of the Killing tensor (i.e., $\nabla_{(\alpha} K_{\mu\nu)} = 0$) and recalling the equations of motion, further reduces to

$$\frac{dQ}{d\tau} = 2K_{\mu\nu} u^\mu u^\nu - 2(\mathcal{L}_z - a\mathcal{E}) \left(\frac{d\mathcal{L}_z}{d\tau} - a \frac{d\mathcal{E}}{d\tau} \right). \quad (\text{C18})$$

The Killing tensor $K^{\mu\nu}$ can be expressed in terms of the Kinnersley basis vectors

$$l^\mu = \frac{1}{\Delta} (\varpi^2, \Delta, 0, a), \quad (\text{C19})$$

$$n^\mu = \frac{1}{2\Sigma} (\varpi^2, -\Delta, 0, a), \quad (\text{C20})$$

$$m^\mu = \frac{1}{\sqrt{2}(r + ia \cos \theta)} (ia \sin \theta, 0, 1, i \csc \theta), \quad (\text{C21})$$

giving

$$K^{\mu\nu} = \Sigma(m^\mu (m^\nu)^* + (m^\mu)^* m^\nu) - a^2 \cos^2 \theta g^{\mu\nu}, \quad (\text{C22})$$

$$= \Sigma(l^\mu n^\nu + n^\mu l^\nu) + r^2 g^{\mu\nu}, \quad (\text{C23})$$

where the star denotes complex conjugation. The equivalency of (C22) and (C23) is clearly demonstrated by expressing the metric in terms of this new basis

$$g^{\mu\nu} = -(l^\mu n^\nu + n^\mu l^\nu) + (m^\mu (m^\nu)^* + (m^\mu)^* m^\nu). \quad (\text{C24})$$

Plugging (C22) into (C18) and multiplying by $\mu/2$, we find that

$$\begin{aligned} \frac{\mu}{2} \frac{dQ}{d\tau} &= q^2 (\mathcal{L}_z \csc^2 \theta - a\mathcal{E}) (f_\varphi + a \sin^2 \theta f_t) \\ &\quad + q^2 u_\theta f_\theta - q^2 (\mathcal{L}_z - a\mathcal{E}) (f_\varphi + a f_t), \end{aligned} \quad (\text{C25})$$

$$\begin{aligned} &= q^2 (\csc^2 \theta \mathcal{L}_z - a\mathcal{E}) (F_\varphi + a \sin^2 \theta F_t) \\ &\quad + q^2 u_\theta F_\theta - q^2 (\mathcal{L}_z - a\mathcal{E}) (F_\varphi + a F_t) \\ &\quad - q^2 (Q - a^2 \cos^2 \theta) u^\alpha F_\alpha. \end{aligned} \quad (\text{C26})$$

Alternatively, plugging (C23) into (C18), we find that

$$\begin{aligned} \frac{\mu}{2} \frac{dQ}{d\tau} &= q^2 \Delta^{-1} (a\mathcal{L}_z - \varpi^2 \mathcal{E}) (a f_\varphi + \varpi^2 f_t) \\ &\quad - q^2 \Delta u_r f_r - q^2 (\mathcal{L}_z - a\mathcal{E}) (f_\varphi + a f_t), \end{aligned} \quad (\text{C27})$$

$$\begin{aligned} &= q^2 \Delta^{-1} (a\mathcal{L}_z - \varpi^2 \mathcal{E}) (a F_\varphi + \varpi^2 F_t) \\ &\quad - q^2 \Delta u_r F_r - q^2 (\mathcal{L}_z - a\mathcal{E}) (F_\varphi + a F_t) \\ &\quad - q^2 (Q + r^2) u^\alpha F_\alpha. \end{aligned} \quad (\text{C28})$$

Regardless of which expression we use, due to the time variation of the rest mass (C1), all four components of the SSF must be known to evaluate $\langle \dot{Q} \rangle$, though the terms proportional to $u^\alpha F_\alpha$ will vanish after taking the orbit average of (C26) and (C28). In this work, we evaluate $\langle \dot{Q} \rangle$ using (C25)–(C28) and check for their consistency as one way of validating our numerical results.

APPENDIX D: FRACTIONAL VARIATIONS OF THE FLUXES

In Table III we report the total fractional variations $\Delta \dot{E}$ and $\Delta \dot{L}_z$, where

TABLE III. Fractional variation in the resonant fluxes for the scalar models listed in Table I. Fractional variations are reported to four decimal places for brevity.

Source	$\Delta \dot{E}^{\mathcal{H}}$	$\Delta \dot{L}_z^{\mathcal{H}}$	$\Delta \dot{E}^\infty$	$\Delta \dot{L}_z^\infty$	$\Delta \dot{E}^{\text{tot}}$	$\Delta \dot{L}_z^{\text{tot}}$
e02.13	0.0011%	0.0004%	0.0001%	0.0002%	0.0001%	0.0003%
e02.12	0.0204%	0.0047%	0.0017%	0.0023%	0.0016%	0.0029%
e02.23	0.2008%	0.0252%	0.0156%	0.0138%	0.0129%	0.0158%
e05.13	1.1214%	0.0400%	0.0109%	0.0227%	0.0092%	0.0287%
e05.12	2.3850%	0.1352%	0.0427%	0.0684%	0.0352%	0.0849%
e05.23	5.8510%	0.3400%	0.1835%	0.1975%	0.1575%	0.2262%

$$\Delta X \equiv 2 \left| \frac{\max[\langle X \rangle] - \min[\langle X \rangle]}{\max[\langle X \rangle] + \min[\langle X \rangle]} \right|. \quad (\text{D1})$$

The total fractional variations primarily increase as p and e increase. In fact, the fractional flux variations for the $e02.13$ orbit are negligible compared to the other sources. This suggests that the dependence of the fluxes on the initial

phase is dampened as a source moves closer to the more massive primary. While $e05.13$ has a smaller pericenter value than $e02.13$, the larger variation in the radial motion could then be responsible for the larger variation in the fluxes with respect to \bar{q}_0 . The behavior of these flux fluctuations and the magnitude their variations is consistent with the gravitational fluxes of [25].

-
- [1] ESA, LISA: We will observe gravitational waves in space, 2021, <https://www.elisascience.org>.
- [2] NASA, LISA: Laser Interferometer Space Antenna, 2021, <http://lisa.nasa.gov>.
- [3] P. Amaro-Seoane *et al.*, *GW Notes* **6**, 4 (2013), <http://astro-gr.org/gw-notes/>; arXiv:1201.3621.
- [4] P. Amaro-Seoane *et al.*, arXiv:1702.00786.
- [5] C. Berry, S. Hughes, C. Sopena, A. Chua, A. Heffernan, K. Holley-Bockelmann, D. Mihaylov, C. Miller, and A. Sesana, *Bull. Am. Astron. Soc.* **51**, 42 (2019), <https://baas.aas.org/pub/2020n3i042>.
- [6] J. Baker *et al.*, arXiv:1907.06482.
- [7] S. Babak, J. Gair, A. Sesana, E. Barausse, C. F. Sopena, C. P. L. Berry, E. Berti, P. Amaro-Seoane, A. Petiteau, and A. Klein, *Phys. Rev. D* **95**, 103012 (2017).
- [8] Y. Mino, *Phys. Rev. D* **67**, 084027 (2003).
- [9] E. Poisson, A. Pound, and I. Vega, *Living Rev. Relativity* **14**, 7 (2011).
- [10] W. Schmidt, *Classical Quant. Grav.* **19**, 2743 (2002).
- [11] S. Drasco, É. É. Flanagan, and S. A. Hughes, *Classical Quant. Grav.* **22**, S801 (2005).
- [12] R. Fujita and W. Hikida, *Classical Quant. Grav.* **26**, 135002 (2009).
- [13] Y. Mino, M. Sasaki, and T. Tanaka, *Phys. Rev. D* **55**, 3457 (1997).
- [14] T. C. Quinn and R. M. Wald, *Phys. Rev. D* **56**, 3381 (1997).
- [15] T. Hinderer and E. E. Flanagan, *Phys. Rev. D* **78**, 064028 (2008).
- [16] U. Ruangsri and S. A. Hughes, *Phys. Rev. D* **89**, 084036 (2014).
- [17] C. P. L. Berry, R. H. Cole, P. Cañizares, and J. R. Gair, *Phys. Rev. D* **94**, 124042 (2016).
- [18] J. Gair, N. Yunes, and C. M. Bender, *J. Math. Phys. (N.Y.)* **53**, 032503 (2012).
- [19] M. van de Meent, *Phys. Rev. D* **89**, 084033 (2014).
- [20] L. Barack and A. Pound, *Rep. Prog. Phys.* **82**, 016904 (2019).
- [21] G. Lukes-Gerakopoulos and V. Witzany, arXiv:2103.06724.
- [22] M. van de Meent, *Phys. Rev. D* **90**, 044027 (2014).
- [23] C. M. Hirata, *Phys. Rev. D* **83**, 104024 (2011).
- [24] E. E. Flanagan and T. Hinderer, *Phys. Rev. Lett.* **109**, 071102 (2012).
- [25] É. E. Flanagan, S. A. Hughes, and U. Ruangsri, *Phys. Rev. D* **89**, 084028 (2014).
- [26] D. P. Mihaylov and J. R. Gair, *J. Math. Phys. (N.Y.)* **58**, 112501 (2017).
- [27] H. Yang and M. Casals, *Phys. Rev. D* **96**, 083015 (2017).
- [28] B. Bonga, H. Yang, and S. A. Hughes, *Phys. Rev. Lett.* **123**, 101103 (2019).
- [29] P. Gupta, B. Bonga, A. J. K. Chua, and T. Tanaka, arXiv:2104.03422.
- [30] M. van de Meent and N. Warburton, *Classical Quant. Grav.* **35**, 144003 (2018).
- [31] L. Speri and J. R. Gair, *Phys. Rev. D* **103**, 124032 (2021).
- [32] S. Isoyama, R. Fujita, H. Nakano, N. Sago, and T. Tanaka, *Prog. Theor. Exp. Phys.* **2013**, 063E01 (2013).
- [33] S. Isoyama, R. Fujita, H. Nakano, N. Sago, and T. Tanaka, *Prog. Theor. Exp. Phys.* **2019**, 013E01 (2019).
- [34] N. Warburton, S. Akcay, L. Barack, J. R. Gair, and N. Sago, *Phys. Rev. D* **85**, 061501(R) (2012).
- [35] T. Osburn, N. Warburton, and C. R. Evans, *Phys. Rev. D* **93**, 064024 (2016).
- [36] N. Warburton, T. Osburn, and C. R. Evans, *Phys. Rev. D* **96**, 084057 (2017).
- [37] A. Pound, B. Wardell, N. Warburton, and J. Miller, *Phys. Rev. Lett.* **124**, 021101 (2020).
- [38] M. van de Meent, *Phys. Rev. D* **97**, 104033 (2018).
- [39] Z. Nasipak, T. Osburn, and C. R. Evans, *Phys. Rev. D* **100**, 064008 (2019).
- [40] C. Misner, K. Thorne, and J. Wheeler, *Gravitation* (Freeman, San Francisco, CA, U.S.A., 1973).
- [41] R. Grossman, J. Levin, and G. Perez-Giz, *Phys. Rev. D* **85**, 023012 (2012).
- [42] B. Carter, *Phys. Rev.* **174**, 1559 (1968).
- [43] S. Drasco and S. A. Hughes, *Phys. Rev. D* **73**, 024027 (2006).
- [44] M. Walker and R. Penrose, *Commun. Math. Phys.* **18**, 265 (1970).
- [45] S. Drasco and S. A. Hughes, *Phys. Rev. D* **69**, 044015 (2004).
- [46] S. Hopper, E. Forseth, T. Osburn, and C. R. Evans, *Phys. Rev. D* **92**, 044048 (2015).
- [47] N. Warburton, L. Barack, and N. Sago, *Phys. Rev. D* **87**, 084012 (2013).
- [48] J. Brink, M. Geyer, and T. Hinderer, *Phys. Rev. D* **91**, 083001 (2015).
- [49] S. Teukolsky, *Astrophys. J.* **185**, 635 (1973).
- [50] T. C. Quinn, *Phys. Rev. D* **62**, 064029 (2000).
- [51] S. L. Detweiler and B. F. Whiting, *Phys. Rev. D* **67**, 024025 (2003).
- [52] L. Barack and A. Ori, *Phys. Rev. D* **61**, 061502(R) (2000).
- [53] L. Barack and A. Ori, *Phys. Rev. Lett.* **90**, 111101 (2003).

- [54] D. R. Brill, P. L. Chrzanowski, C. M. Pereira, E. D. Fackerell, and J. R. Ipser, *Phys. Rev. D* **5**, 1913 (1972).
- [55] L. Barack, A. Ori, and N. Sago, *Phys. Rev. D* **78**, 084021 (2008).
- [56] S. Hopper and C. R. Evans, *Phys. Rev. D* **82**, 084010 (2010).
- [57] N. Warburton and L. Barack, *Phys. Rev. D* **81**, 084039 (2010).
- [58] N. Warburton and L. Barack, *Phys. Rev. D* **83**, 124038 (2011).
- [59] N. Warburton, *Phys. Rev. D* **91**, 024045 (2015).
- [60] D. V. Gal'tsov, *J. Phys. A* **15**, 3737 (1982).
- [61] S. Mano, H. Suzuki, and E. Takasugi, *Prog. Theor. Phys.* **95**, 1079 (1996).
- [62] M. Sasaki and H. Tagoshi, *Living Rev. Relativity* **6**, 6 (2003).
- [63] S. Detweiler, E. Messaritaki, and B. F. Whiting, *Phys. Rev. D* **67**, 104016 (2003).
- [64] A. Heffernan, A. Ottewill, and B. Wardell, *Phys. Rev. D* **89**, 024030 (2014).
- [65] R. Grossman, J. Levin, and G. Perez-Giz, *Phys. Rev. D* **88**, 023002 (2013).
- [66] L. Barack, *Classical Quant. Grav.* **26**, 213001 (2009).
- [67] L. M. Diaz-Rivera, E. Messaritaki, B. F. Whiting, and S. Detweiler, *Phys. Rev. D* **70**, 124018 (2004).
- [68] J. Thornburg and B. Wardell, *Phys. Rev. D* **95**, 084043 (2017).
- [69] Black Hole Perturbation Toolkit, bhptoolkit.org.
- [70] J. Brink, M. Geyer, and T. Hinderer, *Phys. Rev. Lett.* **114**, 081102 (2015).
- [71] M. van de Meent, *Phys. Rev. D* **94**, 044034 (2016).
- [72] T. C. Quinn and R. M. Wald, *Phys. Rev. D* **60**, 064009 (1999).
- [73] C. W. Misner, *Phys. Rev. Lett.* **28**, 994 (1972).
- [74] N. Sago, T. Tanaka, W. Hikida, K. Ganz, and H. Nakano, *Prog. Theor. Phys.* **115**, 873 (2006).
- [75] J. Vines and É. É. Flanagan, *Phys. Rev. D* **92**, 064039 (2015).
- [76] R. Fujita, S. Isoyama, A. Le Tiec, H. Nakano, N. Sago, and T. Tanaka, *Classical Quant. Grav.* **34**, 134001 (2017).
- [77] M. van de Meent and A. G. Shah, *Phys. Rev. D* **92**, 064025 (2015).